Doctoral Dissertation

# Study on Advanced Systems for a Low Power Wide Area Wireless Network of IoT Devices

Faculty of Information Science and Technology
Hokkaido University

**Kanako Yamaguchi**

2020

# Contents

# List of Tables

# List of Figures

# List of Abbreviations

| | |
|---|---|
| 3GPP | Third Generation Partnership Project |
| ACK | ACKnowledge |
| AR | Auto-Regressive |
| AWGN | Additive White Gaussian Noise |
| BS | Base Station |
| BD | Block Diagonalization |
| BER | Bit Error Rate |
| CDF | Cumulative Distribution Function |
| CSS | Chirp Spread Spectrum |
| DBPSK | Differential Binary Phase Shift Keying |
| DSTBC | Differential STBC |
| E-SDM | Eigenbeam-Space Division Multiplexing |
| EHF | Extremely High Frequency |
| eMBB | enhanced Mobile Broadband |
| FSK | Frequency Shift Keying |
| GFSK | Gaussian Frequency Shift Keying |
| IoT | Internet of Things |
| ISM | Industry Science and Medical |
| IStI | Inter-Stream Interference |
| ITU-R | International Telecommunication Union-Radio communication sector |
| IUI | Inter-User Interference |
| LoRa | Long-Range |

| | |
|---|---|
| LOS | Line-of-Sight |
| LPWA | Low-Power Wide-Area |
| LTE-M | Long Term Evolution for Machine type communication |
| M2M | Machine to Machine |
| MFSK | Multiple FSK |
| MIMO | Multi-Input Multi-Output |
| MISO | Multi-Input Single-Output |
| MLD | Maximum Likelihood Detection |
| MMSE | Minimum Mean-Squared Error |
| mMTC | massive Machine Type Communications |
| MRC | Maximum Ratio Combining |
| MS | Mobile Station |
| NB-IoT | Narrow Band-IoT |
| NLOS | Non-LOS |
| OFDM | Orthogonal Frequency Shift Keying |
| PER | Packet Error Rate |
| PN-DSTBC | Power Normalized-DSTBC |
| PI | Phase Interpolation |
| PSK | Phase Shift Keying |
| QAM | Quadrature Amplitude Modulation |
| QPSK | Quadrature Phase Shift Keying |
| RFID | Radio Frequency IDentifier |
| RMS | Root Mean Square |
| RX | Receive |
| SNR | Signal to Noise power Ratio |
| STBC | Space-Time Block Coding |
| SP | Spectral Precoding |
| SVD | Singular Value Decomposition |
| TDD | Time Division Duplexing |
| TX | Transmit |

| | |
|---|---|
| URLLC | Ultra-Reliable and Low Latency communications |
| ZP | Zero-Padding |

# List of Notation

| | |
|---|---|
| $\boldsymbol{a}$ | column vector $\boldsymbol{a}$ (bold-faced small letter) |
| $\boldsymbol{A}$ | matrix $\boldsymbol{A}$ (bold-faced capital letter) |
| $a^*$ | complex conjugate of a scalar $a$ |
| $\boldsymbol{a}^T$ | transpose of $\boldsymbol{a}$ (row vector) |
| $\boldsymbol{A}^T$ | transpose of $\boldsymbol{A}$ |
| $\boldsymbol{a}^H$ | Hermitian transpose of $\boldsymbol{a}$ $(\boldsymbol{a}^H = (\boldsymbol{a}^*)^T)$ |
| $\boldsymbol{A}^H$ | Hermitian transpose of $\boldsymbol{A}$ |
| $\boldsymbol{A}^{-1}$ | inverse of a square matrix $\boldsymbol{A}$ |
| $\boldsymbol{I}_N$ | $N$-dimensional unit matrix |
| $\|\boldsymbol{a}\|$ | vector norm of $\boldsymbol{a}$ |
| $E[\cdot]$ | ensemble average |
| $\boldsymbol{J}_0(\cdot)$ | the Bessel function of the first kind of order zero |
| $\mathcal{Q}(\boldsymbol{x})$ | a quaternion with complex matrix representation of $\boldsymbol{x}$ |
| $\Re(\cdot)$ | real number components |
| $arg(\cdot)$ | the argument of a complex number in $[-\pi, \pi)$ |

# Chapter 1

# Introduction

## 1.1 Background

Since radio communications were first realized in the 19th century, the demand for higher data rate transmission has been growing year after year. According to the Cisco Report [1], the monthly volume of mobile traffic is expected to grow to 77 exabytes by 2022, which is a seven times increase over that of 2017. On the other hand, in recent years, the increase in the number of mobile network devices has been even more remarkable than that of the mobile traffic. Among the contributors to this growth are machine-to-machine (M2M) communications and the Internet of Things (IoT).

In 1999, Kevin Ashton, who is a member of the Auto-ID Center at the Massachusetts Institute of Technology, introduced the "Internet of Things", which is the idea of applying radio frequency identification (RFID) to the supply chain [2], and this was the origin of "IoT". When the concept of the IoT began to be used, RFID was its main objective. However, in 2005, the International Telecommunication Union (ITU) published its first report on IoT and they mentioned that *everything* is a target for IoT as follows: "*Everything from tyres to toothbrushes will fall within communication range, heralding the dawn of a new era, one in which today's internet (of data and people) gives way to tomorrow's Internet of Things.*" [3]. At around the same time as this report was published, smart phones and wearable devices became widespread. Hence, their penetration has led to an explosive increase in the number of network devices. Although the number of M2M connections is only 0.1 per person, the number of devices exceeded the population in around 2008. By 2022, it is expected that 3.6 devices will be connected networks for each person [1].

The explosive expansion of the IoT is changing our lives [4–7]. In recent years, the threat of natural disasters such as earthquakes, typhoons, and in particular extreme weather, has increased. One disaster preparedness/reduction solution is the IoT [8, 9]. In such systems, sensors are placed on mountains, bridges, buildings, at sea, and so on, and constantly

collect data. By analyzing the collected data, an improvement in the accuracy of disaster predictions is achieved. In this way, the IoT reduces the risk of damage due to natural disasters. In the case of a monitoring system, the amount of data transmitted by the sensors to a concentrator is small. Moreover, the transmission frequency is lower than that used for cellular radio. Also, the sensors are placed over a wide area and are driven by batteries. Therefore, the monitoring system needs to achieve both long-range wireless transmission and low power consumption. To satisfy these needs, low-power wide area (LPWA) networks with low energy consumption at low transmission rates are a promising solution [10–13]. Various communication systems, such as LoRa [14] and Sigfox [15] using the industry science and medical (ISM) band and narrow-band IoT (NB-IoT) [16, 17], and long-term evolution equipment utilizing the LTE standard [18], have been supplied for such purpose. In general, a narrow-band system is efficient for long-range wireless transmission. NB-IoT developed by the Third Generation Partnership Project (3GPP) meets the requirements of LPWA networks by using a narrow band width of 180 kHz. Furthermore, constant envelope modulation is also an efficient solution, and Sigfox uses differential binary phase shift keying (DBPSK) and Gaussian frequency shift keying (GFSK) in an ultra-narrow bandwidth of 100 Hz. Thus, Sigfox technology achieves long-range transmission of over 30 to 50 km. In contrast, LoRa technology uses spread spectrum communications by applying chirp spread spectrum (CSS) in order to reduce the required transmit power. As a result, it achieves a maximum transmission range of 10 km.

## 1.2 Objectives of the Dissertation

As described in Section 1.1, LPWA technology is an efficient solution for IoT systems. However, considering the expanding implementation of IoT systems in the future, LPWA technology needs further development [19–22]. In the report on the vision for future wireless communication systems released by the International Telecommunication Union's Radiocommunication Sector (ITU-R) [23], the usage scenarios and requirements are described as follows:

- Ultra-reliable and low latency communications (URLLC)
- Enhanced mobile broadband (eMBB)
- Massive machine type communications (mMTC)

In the future, monitoring systems are expected to provide not only data collection by using sensors but also the control of equipment based on the collected data, for example, smart (electrical) grid and industrial manufacturing. URLLC requires low latency and high reliability to achieve real-time equipment control. According to the Cisco report [1], in recent years, the increase in network traffic has been more rapid than the number of M2M network devices. The cause of the increase is the growth of video applications such as monitoring cameras in IoT systems. Monitoring accelerates the increase of mobile traffic

due to stationary data uploading compared, unlike streaming distribution. As a result, in the case of eMBB, higher data rate transmission and a more efficient utilization of frequency resources are required. The use of mMTC is characterized by a huge number of network devices. It is estimated that a massive number of network devices will be deployed in future IoT systems as they become more widespread. Therefore, future systems will be required to handle many networked devices.

Since the various uses have different features, different solutions are required for each cases. In order to meet the demands of future IoT systems, we investigate enhanced solutions which will achieve "high reliability transmission", "high data rate transmission", and "multi-user transmission", for the conventional LPWA technology in terms of the physical layer.

### 1.2.1 High reliability transmission

As mentioned in Section 1.1, narrow-band constant-envelope modulation is effective for long-range wireless transmission. Continuous-phase frequency shift keying (FSK) is a power-efficient modulation scheme with less envelope fluctuation than phase shift keying (PSK) and quadrature amplitude modulation (QAM). In terms of range extension, a diversity strategy is effective for increasing the communication quality in a fading environment. Space-time block coding (STBC), which is a spatial diversity scheme, exploits the diversity gain fully in spite of its simple configuration [24]. Moreover, coherent detection achieves longer range transmission than envelope detection.

Coherent FSK with STBC is a promising candidate for long-range, high reliability wireless transmission [25]. However, a straightforward implementation of STBC for FSK breaks the constant-envelope property because the sign reversal in an STBC block causes a phase discontinuity between the FSK symbols. In that case, the trajectory of the STBC output signal crosses near to zero. Therefore, the power efficiency decreases due to the increased envelope fluctuation of the STBC output signal, despite using FSK to reduce the envelope fluctuation. In general, estimation of the channel parameters is necessary for coherent detection, and the accuracy of the channel estimation has an effect on the detection performance in mobile communications. However, since pilot symbols are needed to estimate the channel parameters, coherent detection reduces the transmission efficiency.

In order to resolve the above issues and achieve long-range wireless communications with high reliability, we propose a narrow-band pilot-less coherent FSK transmission system using phase rotated transmit diversity. The pilot-less coherent FSK scheme estimates the channel responses instantaneously at the first sample of each FSK symbol by utilizing the feature that the initial phase of an FSK symbol is uniquely determined under certain conditions, and interpolates between the channel estimates using Lagrange interpolation [26]. The phase rotated transmit diversity scheme, which is an alternative STBC with phase rotation, equalizes the amplitude across the transmit antennas and suppresses the envelope fluctuation by controlling the phase trajectory between the FSK symbols. By using computer simulations, we verify that the proposed system improves the transmit power

efficiency and the performance at each Doppler frequency compared to a conventional scheme.

### 1.2.2 High data rate transmission

Multi-level modulations and extremely high frequency (EHF) radio communications at radio frequencies of 30 to 300 GHz are suitable for satisfying the demand for higher data rate transmission [27, 28]. On the other hand, the transmission range is reduced due to the increase in the required transmit power in the high-level modulation case and the effect of phase noise in the EHF band.

In order to address the above issues, two-dimensional diversity which exploits frequency and spatial diversity simultaneously by serially concatenating multicarrier spreading and STBC is an efficient approach [29]. However, since the multicarrier spreading approach degrades the spectral efficiency, an alternative frequency diversity approach is needed for higher-data rate transmission. Spectral precoding uses linear algebraic rotation in the frequency domain to transmit precoded signals at different frequencies. This technique is able to exploit frequency diversity gain without loss of spectral efficiency in return for increased computational complexity [30]. On the other hand, differential STBC (DSTBC) is an attractive spatial diversity scheme for reducing the signal fluctuation due to fading as well as the severe effects of oscillator phase noise in the EHF band [31]. Moreover, power-normalized-DSTBC (PN-DSTBC) has been proposed for multi-level modulation such as QAM to mitigate the amplitude variance of differentially-encoded symbols [32], and its effectiveness has been demonstrated even in a high-order QAM case [33].

In order to increase the communication capacity and further maintain the transmission range, we investigate an alternative two-dimensional diversity approach concatenated with spectral precoding (SP) and PN-DSTBC. In the case of a naive concatenation of SP and PN-DSTBC, the imbalance of the equivalent noise variances over the transmit frequencies at the PN-DSTBC decoder output affects the spectral decoder performance. Hence, we propose a modified approach which compensates the equivalent noise imbalance by using an equalized PN-DSTBC decoder to address this issue, and verify the performance improvement of the proposed approach by using computer simulations.

### 1.2.3 Multi-user transmission

For the down link transmission scenario in a multi-user multiple-input multiple-output (MIMO) system, a base station (BS) simultaneously sends signals to multiple users. Thus, we may encounter inter-user interference (IUI) that can seriously degrade the performance and the transmission range. A block diagonalization (BD) scheme can be applied to eliminate IUI [34, 35]. This scheme block-diagonalizes the multi-user MIMO channels, and forces the interference to other users to become zero. Although IUI can be suppressed by using a BD scheme, inter-stream interference (IStI) occurs because the BS may transmit multiple streams to each mobile station (MS). We can suppress IStI by using eigenbeam-space

division multiplexing (E-SDM) [36] that partitions the MIMO channels into orthogonal channels by forming eigenbeams. The transmitter needs to be able to distinguish the beamforming weights from the channel responses for these techniques to be used.

The propagation environments in wireless communication systems vary over time. The MIMO channels change during the time between when the transmit parameters are determined and the actual MIMO transmission in a time-varying environment, such that the transmission weights are no longer optimum [37]. Hence, the performance is seriously degraded because we cannot suppress the interference by using the outdated beamforming weights. Channel prediction [38–43] techniques can be used to mitigate the effects of outdated channel responses. One typical scheme is a linear predictor based on the autoregressive (AR) model [44]. The predictor needs AR coefficients determined from the Yule-Walker equation to predict future channels. The autocorrelations of the channels are needed to obtain the Yule-Walker equation. Since many data points are required, the channel autocorrelations are not easy to estimate accurately in real-life environments. Thus far, we have calculated the autocorrelations assuming the Jakes' model [45,46]. However, even in this case, we need the maximum Doppler frequency to obtain the autocorrelations. It is not necessarily easy to accurately estimate values for the maximum Doppler frequency in real-life environments. In contrast, the Lagrange extrapolation scheme [47, 48] can predict future channels without parameters such as autocorrelations or the maximum Doppler frequency. This method can predict future channels by simple extrapolation using past channels alone. As a result, we can easily implement the Lagrange scheme.

Reference [37] describes the channel prediction effect for the multi-user MIMO system. The evaluations were, however, limited to a linear case of the Lagrange extrapolation. The prediction performance degrades depending on the time variations. Also, ideal channel estimation was assumed and channel estimation error due to receiver noise was not taken into account. Based on the previous work, we examined what effects AR-model-based prediction and the type of Lagrange extrapolation (linear, second-order, and third-order extrapolations) had on multi-user MIMO downlink transmission. We evaluated the performance in cases of the Jakes' model and an actual indoor environment. The MIMO channels were estimated using finite pilot symbols, and the evaluations were done in the presence of channel estimation errors.

## 1.3 Contents of the Dissertation

The outline of the dissertation is illustrated in Fig. 1.1. In Chapter 2[1], the author proposes a pilot-less narrow-band coherent FSK system using phase rotated transmit diversity as a high reliability long-range transmission system. The phase rotated transmit diversity scheme reduces the phase discontinuity between the space-time bounded FSK symbols, and therefore suppresses any envelope fluctuations. The proposed pilot-less coherent FSK

[1]Chapter 2 is based on "A Pilot-less Narrowband Coherent FSK System using Phase Rotated Transmit Diversity with Suppression of Envelope Fluctuation" [49], by the same author, which appeared in IEICE Trans. Commun. (Japanese Edition), vol.J102-B, no.2, pp.100–109, Copyright©2020.

scheme estimates the channel parameters by using the feature that the initial phase of an FSK symbol is uniquely determined, instead of inserting known pilot symbols. The performance evaluation by computer simulation shows that the proposed scheme improves the transmit power efficiency compared to conventional STBC. Furthermore, the proposed scheme shows improved performance even in the event of rapid movement.

The next chapter[2] examines a two-dimensional diversity approach by serially concatenating SP and PN-DSTBC to achieve high data rate transmission. First, the author reveals the problem that a naive concatenation degrades the performance due to the imbalance of the equivalent noise variances over the transmit frequencies. Thus, the author proposes an equalized PN-DSTBC decoder as a modified approach to uniform equivalent noise variances over the frequencies. The performance evaluation using computer simulations shows that the proposed modified approach provides performance improvement with any modulation schemes and at any number of transmit frequencies.

Chapter 4[3] considers a multi-user MIMO system. In this case, although the BS obtains suppression of the interference by using transmit weights based on the channel responses, the outdated channels seriously affect the performance. Therefore, the author applies channel prediction schemes, AR-model based prediction and Lagrange extrapolation, in order to mitigate this effect. Using indoor measurement data, the author evaluates the performance in different time-varying environments, and it is shown that the proposed channel prediction schemes can improve the performance.

Finally, the author summarizes all the studies in the dissertation and draws conclusions in Chapter 5. In addition, future work that should be considered and tackled for prospective IoT systems is briefly discussed.

[2]Chapter 3 is based on "An Equalization of PN-DSTBC for Concatenating with Spectral Precoding" [50], by the same author, which appeared in IEICE Trans. Fundamentals vol.E102-A, no.3, pp.544–552, Copyright©2019 IEICE.

[3]Chapter 4 is based on "Channel Prediction Techniques for a Multi-User MIMO System in Time-Varying Environments" [51], by the same author, which appeared in IEICE Trans. Commun., vol.E97-B, no.12, pp.2747–2755, Copyright©2014 IEICE.

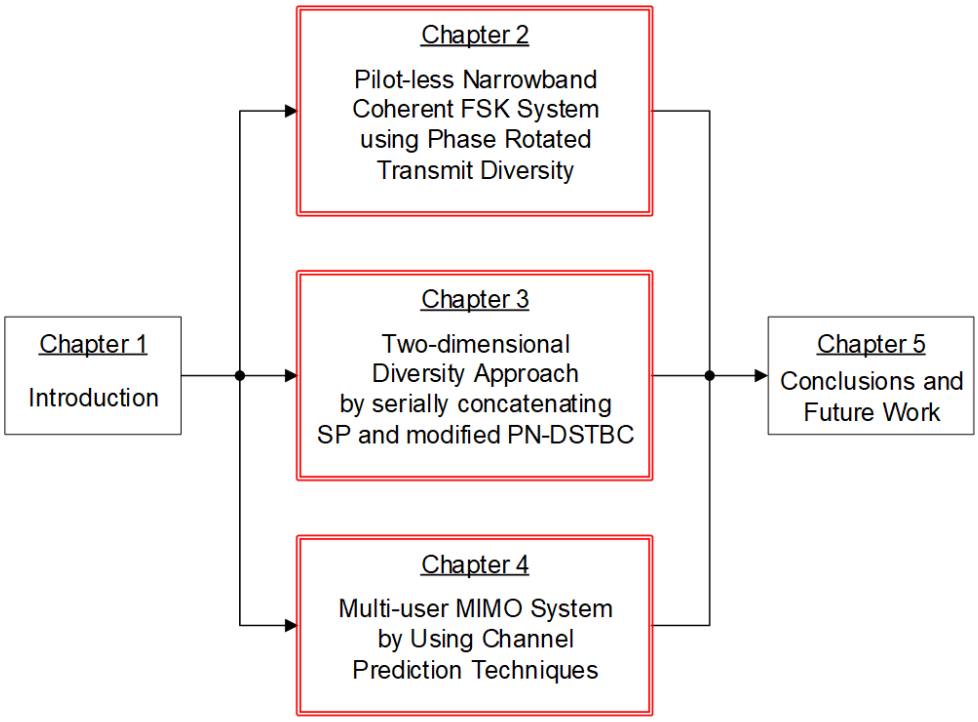


Figure 1.1: Outline of the dissertation.

# Chapter 2

# Pilot-less Narrow-band Coherent FSK System using Phase Rotated Transmit Diversity

This chapter proposes a pilot-less narrow-band FSK system applying phase rotated transmit diversity with suppression of envelope fluctuation as high-reliable transmission technique.

## 2.1 Proposed system

### 2.1.1 Space-Time Block Coding scheme

A diversity strategy is effective for realizing the high reliability transmission, and STBC, which is one of a spatial diversity scheme, achieves the full diversity gain by the simple linear processing. Then, in this chapter, the author applies STBC to the proposed system to increase the communication quality.

In STBC scheme, the encoding is done in space and time to achieve transmit diversity. The STBC signal matrix with two transmit antennas is given by

$$\begin{bmatrix} z^{(1)}(1) & z^{(1)}(2) \\ z^{(2)}(1) & z^{(2)}(2) \end{bmatrix} = \begin{bmatrix} s(1) & -s^*(2) \\ s(2) & s^*(1) \end{bmatrix}, \tag{2.1}$$

where $(\cdot)^*$ indicates complex conjugate, $s(j)$ denotes a modulated signal, $z^{(k)}(j)$ denotes an STBC signal, $j$ is a symbol index of the STBC block $(j = 1, 2)$, and $k$ is the index of a transmit antenna $(k = 1, 2)$.

For the sake of simplicity, it is assumed that the channel between the transmit antenna and the received antenna is constant during the STBC block and the number of received

antenna is one. Then, the received signals are given by

$$\begin{aligned}\begin{bmatrix} r(1) \\ r(2) \end{bmatrix} &= \begin{bmatrix} h^{(1)}z^{(1)}(1) + h^{(2)}z^{(2)}(1) + n(1) \\ h^{(1)}z^{(1)}(2) + h^{(2)}z^{(2)}(2) + n(2) \end{bmatrix} \\ &= \begin{bmatrix} h^{(1)}s(1) + h^{(2)}s(2) + n(1) \\ -h^{(1)}s^*(2) + h^{(2)}s^*(1) + n(2) \end{bmatrix}. \end{aligned} \tag{2.2}$$

Here, $r(j)$ indicates a received signal at $j$-th symbol of STBC block, and $n(j)$ denotes an additive white Gaussian noise (AWGN) component. At the receiver, the decoded signal $\tilde{s}(j)$ is obtained by using linear processes thanks to the orthogonality of the STBC coding as shown in (2.1), and we have

$$\begin{aligned}\begin{bmatrix} \tilde{s}(1) \\ \tilde{s}(2) \end{bmatrix} &= \begin{bmatrix} r(1)h^{*(1)} + r^*(2)h^{(2)} \\ r(1)h^{*(2)} - r^*(2)h^{(1)} \end{bmatrix} \\ &= \begin{bmatrix} (|h^{(1)}|^2 + |h^{(2)}|^2)s(1) + h^{(1)*}n(1) + h^{(2)}n^*(2) \\ (|h^{(1)}|^2 + |h^{(2)}|^2)s(2) + h^{(2)*}n(1) - h^{(1)}n^*(2) \end{bmatrix}. \end{aligned} \tag{2.3}$$

From (2.3), an instantaneous signal to noise power ratio (SNR) is given by

$$\begin{aligned}\mathrm{SNR} &= \frac{(|h^{(1)}|^2 + |h^{(2)}|^2)^2 P_S}{(|h^{(1)}|^2 + |h^{(2)}|^2)P_N} \\ &= (|h^{(1)}|^2 + |h^{(2)}|^2)\frac{P_S}{P_N}, \end{aligned} \tag{2.4}$$

where $P_S$ and $P_N$ indicate an instantaneous signal power and noise power, respectively. As shown in (2.4), the STBC decoder obtains two-branch transmit diversity gain. It is noted that STBC achieves the same diversity order as the maximal ratio combining (MRC) with two receive antennas although STBC has a 3 dB penalty of SNR compared to that of MRC when the total transmit power is equal between STBC and MRC.

### 2.1.2 Transmitter

Figure 2.1 shows the proposed system model of the proposed transmitter which employs two transmit antennas. First, at the transmitter, a multiple FSK (MFSK) modulator selects one FSK carrier from a set of $M$ orthogonal FSK carriers depending on the input coded data bits, and then a time domain symbol is generated. The time domain symbol $s(m, n)$ is given by

$$s(m, n) = \exp\left(j\frac{2\pi}{M} \cdot \gamma \cdot (m-1) \cdot c(n).\right) \tag{2.5}$$

Here, $m$ is a sample index $(0 < m \leq M)$ in an FSK symbol, $n$ is the FSK index $(0 < n \leq N)$ in the frame, $\gamma$ is the FSK modulation index $(0 < \gamma \leq 1)$, and $c(n)$ is the transmit carrier index. After that, in order to achieve the high reliability network, STBC is applied

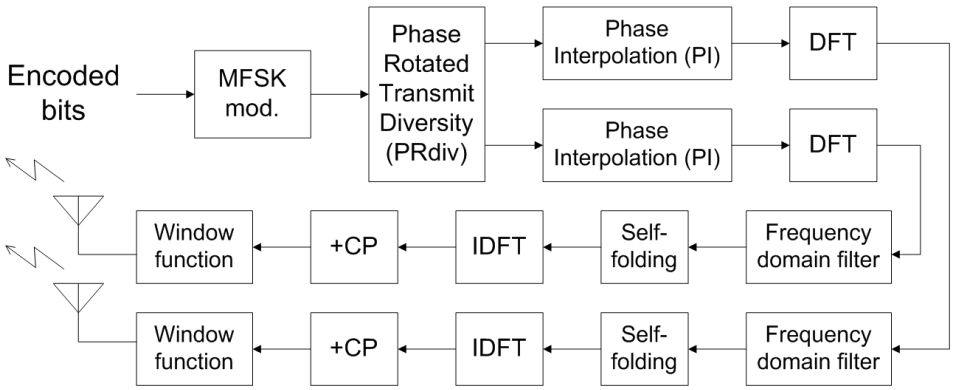


Figure 2.1: Proposed system model (transmitter).

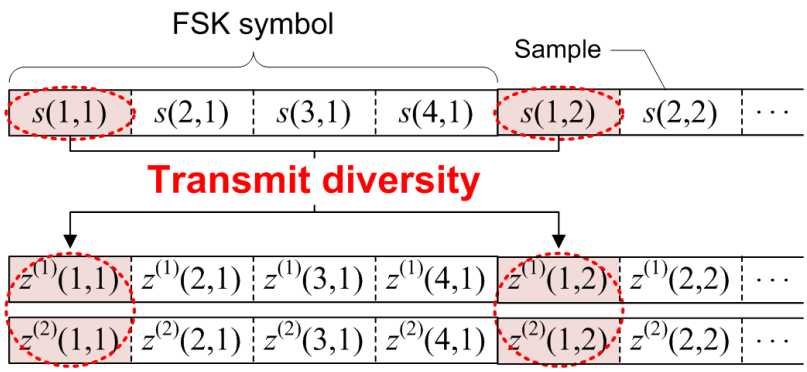


Figure 2.2: STBC block format.

to the modulated signal between the FSK symbols as shown in Fig. 2.2. The conventional STBC signal as described in [24] is given by

$$\begin{bmatrix} z^{(1)}(m,2i-1) & z^{(1)}(m,2i) \\ z^{(2)}(m,2i-1) & z^{(2)}(m,2i) \end{bmatrix} = \begin{bmatrix} s(m,2i-1) & -s^*(m,2i) \\ s(m,2i) & s^*(m,2i-1) \end{bmatrix}. \tag{2.6}$$

Here, $z^{(k)}(m,n)$ denotes an STBC signal and $i$ is an STBC block's index $(0 < i \leq N/2)$. As shown in (2.6), the STBC signals of the transmit antenna $k = 1$ (referred to as "TX1") reverse the sign at each FSK symbol. When FSK modulation is employed, the modulated signal keeps the envelope fluctuation. However, due to the sign reversal in conventional STBC as shown in (2.6), the trajectory of the STBC output crosses near to zero between the FSK symbols at TX1. Therefore, the envelope fluctuation from one transmit antenna increases, and the transmit power efficiency degrades.

Hence, we propose a phase rotated transmit diversity technique which suppresses the envelope fluctuation by adding a phase rotation to the STBC in each FSK symbol. Here,

Table 2.1: Signal constellation pattern.

| | Phase rotation | Oversampling method | Caption |
|---|---|---|---|
| Fig. 3 | None (STBC) | Zero-padding (ZP) | STBC + ZP |
| Fig. 4 | None (STBC) | Phase interpolation (PI) | STBC + PI |
| Fig. 5 | Applying (PRdiv) | Zero-padding (ZP) | PRdiv + ZP |
| Fig. 6 | Applying (PRdiv) | Phase interpolation (PI) | Proposed |

the proposed STBC signal with phase rotation $\theta$ is given by

$$\begin{bmatrix} z^{(1)}(m,2i-1) & z^{(1)}(m,2i) \\ z^{(2)}(m,2i-1) & z^{(2)}(m,2i) \end{bmatrix} = \begin{bmatrix} s(m,2i-1)\times \mathrm{e}^{j(2i-1)\theta} & -s^*(m,2i)\times \mathrm{e}^{j2i\theta} \\ s(m,2i)\times \mathrm{e}^{j(2i-1)\theta} & s^*(m,2i-1)\times \mathrm{e}^{j2i\theta} \end{bmatrix}. \tag{2.7}$$

The phase rotation in (2.7) suppresses the envelope fluctuation which is caused by the sign reversal, which maintaining the orthogonality of the STBC. Note that the proposed phase rotation technique to a case with more than two transmit antennas.

Oversampling and spectrum shaped filtering are necessary for implementation of this approach. When the coded signal given in (2.7) is oversampled by zero-padding (ZP) at the points of time-domain filtering, the filtered signal loses its constant envelope property resulting in degradation of the transmit power efficiency even when the proposed transmit diversity is applied. Therefore, as the oversampling method in the proposed system, we apply a phase interpolation (PI) which inserts signals with the same amplitude as the original signal while maintaining the constant envelope [52]. At the point of phase interpolation, the STBC signal is oversampled with a factor $V$, and thus we obtain the oversampled version of the STBC signal:

$$z^{(k)}_{\mathrm{ovs}}((mV-V+v),n) = z^{(k)}(m,n) \times \mathrm{e}^{j(\arg(z^{(k)}(m,n)\cdot z^{(k)}(m+1,n)v/V))}. \tag{2.8}$$

Here, $\arg(\cdot)$ denotes the argument of a complex number in $[-\pi,\pi)$, and $v$ is an oversample index $(0 < v \leq V)$.

Figure 2.3∼2.6 show the signal constellation and trajectory when the phase rotation and the oversampling method are changed. Moreover, Tab. 2.1 shows a signal constellation pattern of the phase rotation and the oversampling method. In the following discussion, we refer the transmit diversity technique without the phase rotation and with it as “STBC” and “PRdiv”, respectively. Here, the modulation scheme is 4FSK, a root Nyquist filter with roll-off factor $\alpha = 0.2$ is applied, and the phase rotation of PRdiv $\theta$ is $\pi/2$. First, we compare the difference of the signal constellation due to the oversampling method. As can be seen in Fig. 2.3 and 2.4, when STBC is applied as the transmit diversity, the envelope fluctuation is reduced by applying PI at TX2. On the other hand, at TX1, we can see the trajectory crossing near to zero and the envelope fluctuation is increased caused by the sign reversal in STBC code given by (2.6). Next, let us compare the diversity method. When

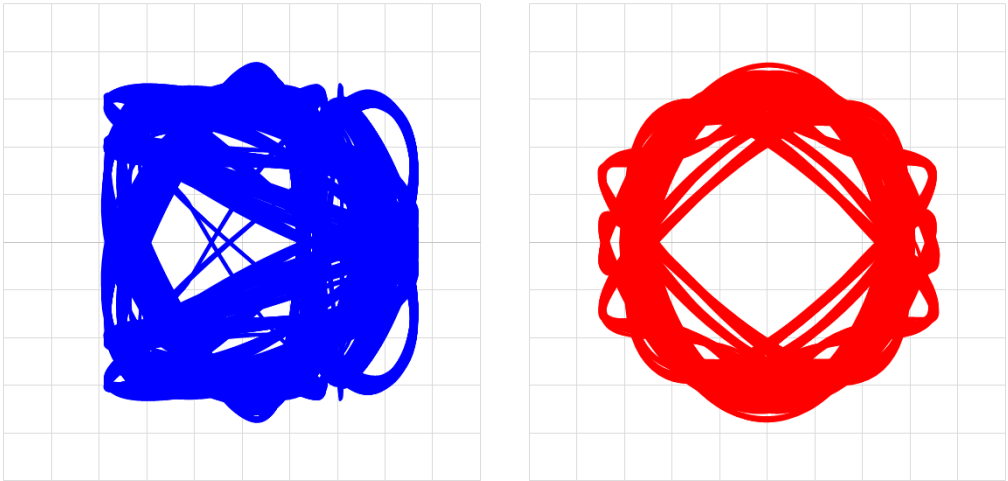

(a) TX1 (b) TX2

Figure 2.3: Signal constellation and trajectory (STBC + ZP).

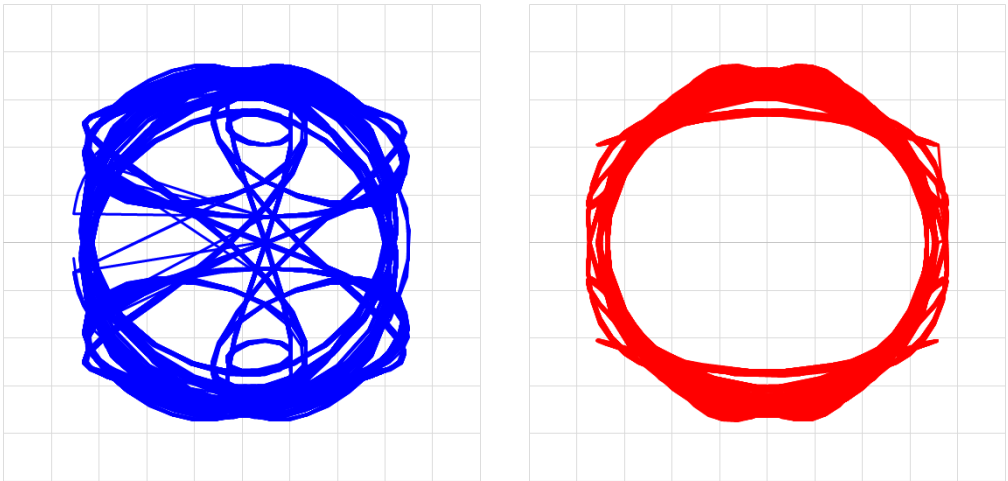

(a) TX1 (b) TX2

Figure 2.4: Signal constellation and trajectory (STBC + PI).

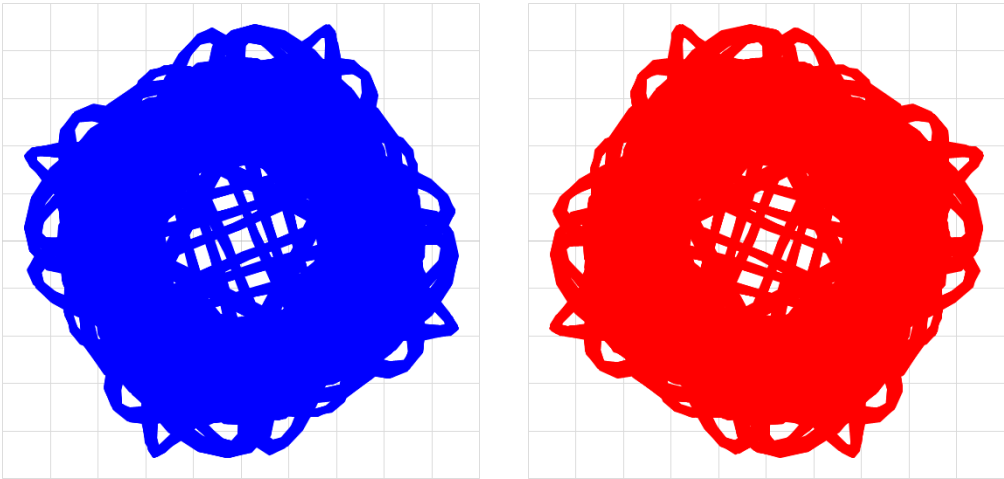

(a) TX1 (b) TX2

Figure 2.5: Signal constellation and trajectory (PRdiv + ZP, $\theta = \pi/2$).

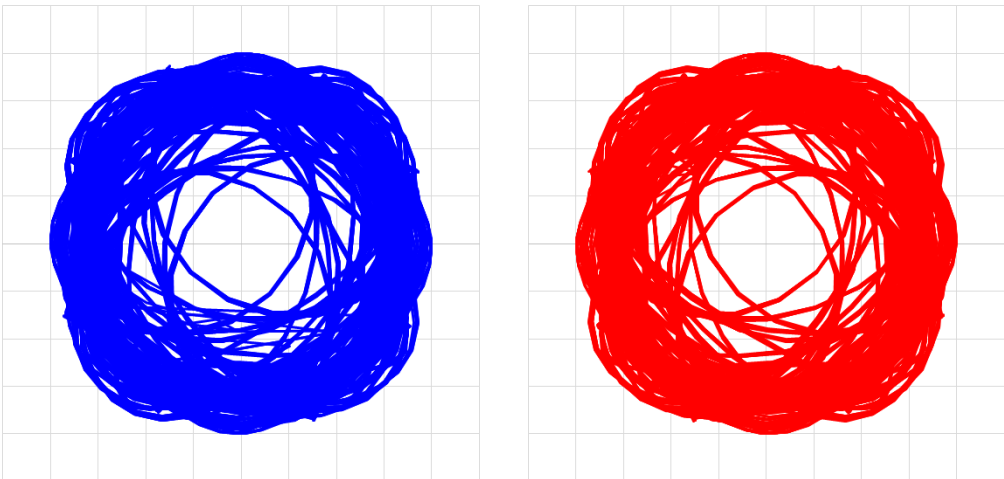

(a) TX1 (b) TX2

Figure 2.6: Signal constellation and trajectory (Proposed scheme, $\theta = \pi/2$).

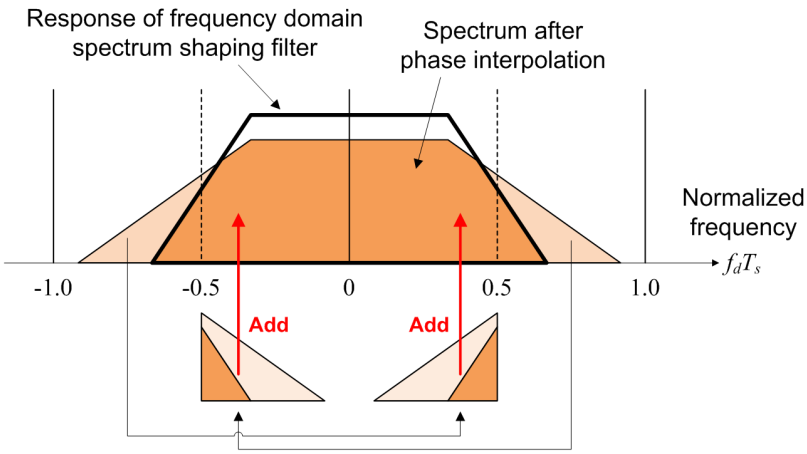


Figure 2.7: Schematic drawing of the self-folding operation ($V$=2).

comparing Fig. 2.3 and Fig. 2.5, Fig. 2.4 and Fig. 2.6, respectively, the transmit signal follows a circular track at each transmit antenna in the case of PRdiv. Moreover, PRdiv eliminates periodic dropping of the amplitude into zero. As given in (2.7), PRdiv which employs the phase rotation reduces the effect of the phase trajectory caused by the sign reverse in STBC code. Furthermore, in the case where PI is applied as the oversampling method, the envelope fluctuation is reduced.

When each transmit block consists of $U$ FSK symbols, the oversampled signal $z_{\mathrm{ovs}}^{(k)}((mV-V+v),n)$ transforms to the frequency domain by means of discrete Fourier transform (DFT) with $N_{DFT} = UMV$ points. Then, a root Nyquist filter is applied to the oversampled signals as a band-limiting filter. The root roll-off filter is designed based on the Nyquist rate and has a bandwidth $f$. On the other hand, the bandwidth of $z_{\mathrm{ovs}}^{(k)}((mV - V + v), n)$ is $fV$ due to the oversampling with phase interpolation. As a result, the filtered spectrum is distorted due to the mismatch between the occupied bandwidth of the filter input and the filter response that results in a performance degradation. Therefore, in the proposed system, the spectrum shaping uses an analogy from the sampling theorem, and we call this a self-folding operation [52]. Figure 2.7 shows a representation of the self-folding operation. As shown in Fig. 2.7, the spectrum after the phase interpolation is widened and the widening is removed by the band-limiting filter, resulting in pulse distortion. The filtered signal is converted to a time domain signal by inverse DFT (IDFT) with $N_{DFT}$ points. Finally, a cyclic prefix (CP) is added to the filtered signal and a windowing technique [53] is applied to create phase continuity between the transmission blocks.

### 2.1.3 Receiver

Figure 2.8 shows the proposed system model at the receiver side. At the receiver, a receive filter is applied to the received signal and synchronization is performed to detect the trans-

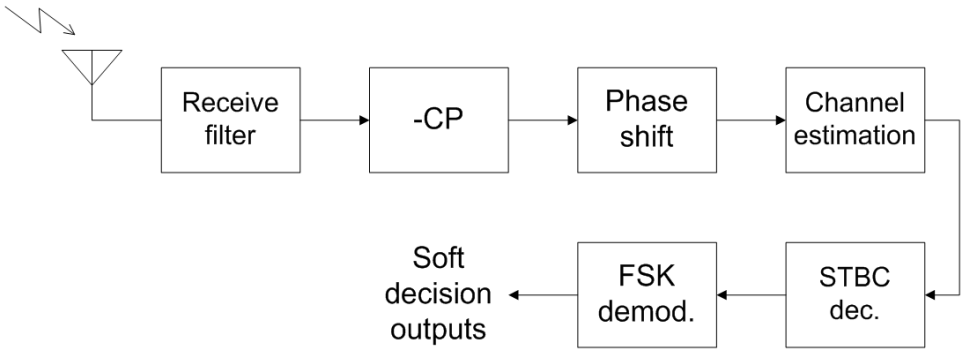


Figure 2.8: Proposed system model (receiver).

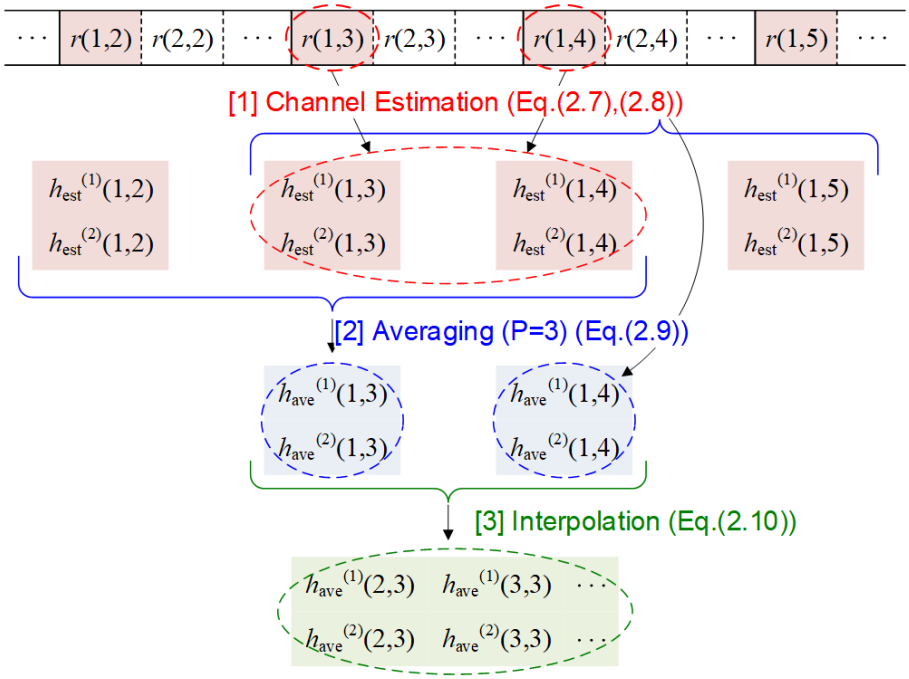


Figure 2.9: Representation of the channel estimation (4FSK, $P$=3).

mission block timing and the frequency offset between the transmitter and the receiver. After the received filter and the synchronization, the received signal at the FSK sample rate

is given by

$$\begin{bmatrix} r(m,2i-1) \\ r(m,2i) \end{bmatrix} = \begin{bmatrix} (h^{(1)}(m,2i-1)s(m,2i-1)+h^{(2)}(m,2i-1)s(m,2i)) \\ \quad \times \mathrm{e}^{j(2i-1)\theta}+\eta(m,2i-1) \\ (-h^{(1)}(m,2i)s^{*}(m,2i)+h^{(2)}(m,2i)s^{*}(m,2i-1)) \\ \quad \times \mathrm{e}^{j2i\theta}+\eta(m,2i) \end{bmatrix}, \tag{2.9}$$

where $h^{(k)}(m,n)$ denotes the channel response between the $k$-th transmit antenna and the receive antenna, and $\eta(m,n)$ indicates an AWGN component. In order to remove the phase rotation introduced by the proposed STBC, a phase shift is performed and the shifted signal is given by

$$[\, r(m,2i-1)\times \mathrm{e}^{-j(2i-1)\theta} \quad r(m,2i)\times \mathrm{e}^{-j2i\theta}\,]^{T}. \tag{2.10}$$

The pilot-less channel estimation is carried out after removing the CP and rotating the phase. As given in (2.5), the initial phase of an FSK symbol $(m=1)$ is uniquely determined when the FSK modulation index $\gamma$ is 1.0 regardless of the transmit carrier index $c(n)$. Therefore, the proposed system obtains the estimated channel responses by using the initial sample of each FSK symbol as the pilot sample for the channel estimation. Since the proposed scheme does not insert the known pilot symbol for channel estimation, it estimates the channel responses without decreasing the transmission rate. The pilot-less channel estimation is carried out after removing the CP and rotating the phase. As given in (2.5), the initial phase of an FSK symbol $(m=1)$ is uniquely determined when the FSK modulation index $\gamma=1.0$ regardless of the carrier index $c(n)$. Therefore, the proposed system obtains the estimated channel responses by using the initial sample of each FSK symbol as the pilot sample for the channel estimation. Then, the proposed system achieves the channel estimation without reducing a transmission rate because it is not required to insert the known pilot symbol. Figure 2.9 shows a representation of the proposed channel estimation in the case where the modulation scheme is 4FSK and the number of averaging $P$=3. Here, the channel responses are settled within the STBC block. The estimated channel responses at initial sample $(m=1)$ are given by

$$h^{(1)}_{\mathrm{est}}(1,2i-1)=h^{(1)}_{\mathrm{est}}(1,2i)=\frac{r(1,2i-1)-r(1,2i)}{2}, \tag{2.11}$$

$$h^{(2)}_{\mathrm{est}}(1,2i-1)=h^{(2)}_{\mathrm{est}}(1,2i)=\frac{r(1,2i-1)+r(1,2i)}{2}, \tag{2.12}$$

where $h^{(k)}_{\mathrm{est}}(1,n)$ denotes the estimated channel. Next,in order to mitigate the effects of noise, the estimated value is averaged across weighted FSK symbols, and we have

$$h^{(k)}_{\mathrm{ave}}(1,n)=\frac{\sum_{p=1}^{P} w_p h^{(k)}_{\mathrm{est}}\left(1,n-\frac{P+1}{2}+p\right)}{P}. \tag{2.13}$$

Here, $h_{\text{ave}}^{(k)}(m,n)$ denotes the averaged channel value, $P$ is the number of averages taken, and $w_p$ denotes the weighting coefficient, increasing towards the target symbol $n$. After that, we apply 1st-order Lagrange interpolation [26] to obtain an estimated channel value at each sample by using the averaged channel as

$$\tilde{h}^{(k)}(m,n) = h_{\text{ave}}^{(k)}(1,n) + \frac{m}{MV}(h_{\text{ave}}^{(k)}(1,n+1) - h_{\text{ave}}^{(k)}(1,n)), \tag{2.14}$$

where $\tilde{h}^{(k)}(m,n)$ denotes the estimated channel value. The conventional STBC decoding is applied to the received signal by using the estimated channel responses as in (2.14).

Coherent demodulation in the frequency domain is performed to detect the FSK symbols and to provide a soft-decision output for a decoder. As we discussed earlier, an MFSK symbol has $M$ samples and is defined from $M$ carriers. In the MFSK demodulator, DFT with $M$ points is performed on the received MFSK symbols to obtain their frequency domain representations. The FSK carrier which has the largest in-phase amplitude among the $M$ FSK carriers is selected for the estimated of the transmitted FSK symbols. The soft-decision output is calculated from the in-phase amplitude of each FSK carrier [54].

## 2.2 Performance Evaluation

### 2.2.1 PAPR Performance

Figure 2.10 plots the normalized instantaneous power versus the cumulative distribution function (CDF) in the cased of the proposed transmit scheme. Here, the normalized instantaneous power is defined as the instantaneous FSK oversampled power divided by the average oversampled power at the TX filter output. As described before, the constant envelope improves the power efficiency, namely, the normalized instantaneous power is 0 dB which indicates that the peak power coincides with the average power giving the best performance as shown in Fig. 2.10. The simulation conditions are the same as in Fig. 2.3∼2.6, and a frame consists of a block, where each block consists of eight symbols without CP. As shown in Fig. 2.10, by comparing STBC+ZP (Fig. 2.3) and STBC+PI (Fig. 2.4), the envelope fluctuation of PI is less than that of ZP and it indicates the better performance at TX2. On the other hand, at TX1, a deviation value from the normalized instantaneous power $= 0$ dB increases due to the sign reversal in the STBC code. When comparing the transmit diversity schemes, the case of PRdiv yields the same performance at each transmit antenna. We can see that PRdiv achieves an improvement of the deviation values from the normalized instantaneous power $= 0$ dB about 2 dB from -10 dB of STBC+ZP (Fig. 2.3) to -8 dB of PRdiv+ZP (Fig. 2.5) and 10 dB from -16 dB of STBC+PI (Fig. 2.4) to -6 dB of Proposed (Fig. 2.6). Moreover, Proposed (Fig. 2.6) suppresses the deviation of the normalized instantaneous power by about 2 dB compared with that of ZP+PRdiv (Fig. 2.5).

Next, we evaluate the phase rotation $\theta$ of the proposed phase rotated transmit diversity given by (2.7) which yields the best transmit power efficiency. Figure 2.11 plots the normalized instantaneous power by changing the phase rotation $\theta$. In general, since each

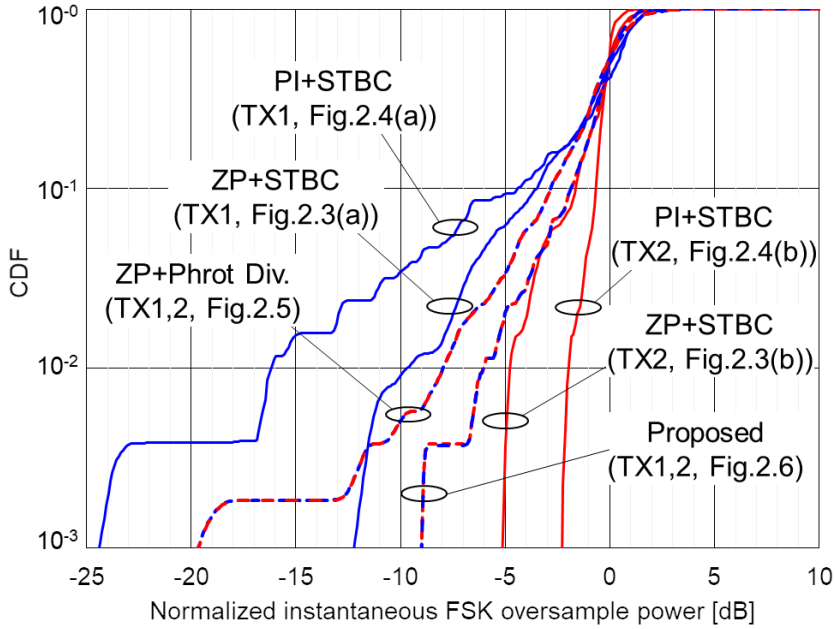


Figure 2.10: Normalized instantaneous power performance (4FSK).

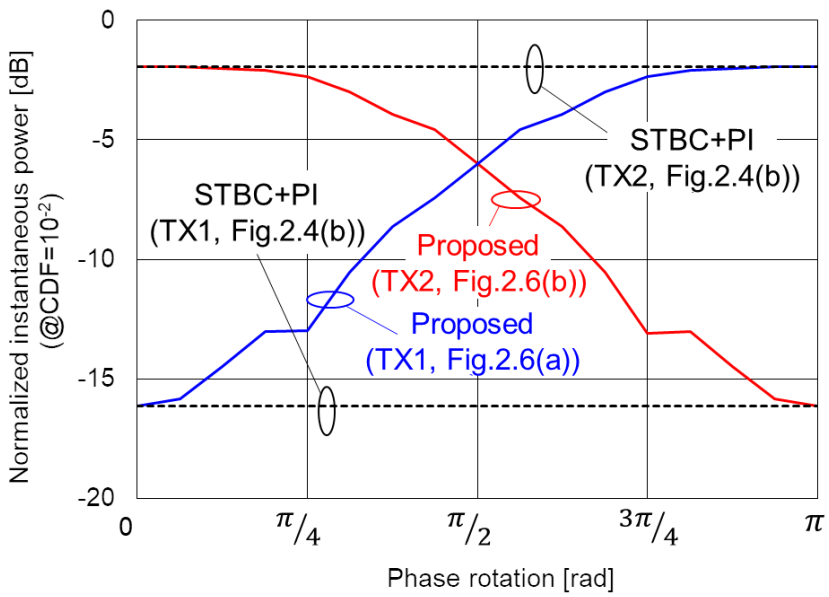


Figure 2.11: Normalized instantaneous power performance by changing $\theta$ (CDF=$10^{-2}$).

Table 2.2: Simulation parameters.

| | |
|---|---|
| No. of antennas | TX:2, RX:1 |
| Modulation scheme | 4FSK<br>(Modulation index: $\gamma$ = 1.0) |
| Frame configuration | Frame length: 10 blocks<br>Block length: 8 symbols |
| CP length | 8 samples (at oversampling rate) |
| Band-limiting filter | Root roll-off filter<br>(Roll-off factor: $\alpha = 0.2$) |
| Window function | Hanning-window |
| Oversampling factor | $V$ = 8 |
| Error correcting code | Convolutional code ($R$=1/2, $K$=7)<br>Soft-decision viterbi decoding |
| Phase rotation | $\theta = \pi/2$ |
| No. of averaging symbols | $P = 1$ $(w_1 = 1)$<br>$P = 3$ $(w_1 = w_3 = 1, w_2 = 2)$<br>$P = 5$ $(w_1 = w_5 = 1, w_2 = w_4 = 2, w_3 = 3)$ |

antenna is applied the same amplifier within a common system, it is fixed based on the maximum deviation of the normalized instantaneous power of the system. Hence, in Fig. 2.11, the phase rotation $\theta$ minimizing a deviation from the normalized instantaneous power $= 0$ dB at the transmit antenna which yields the maximum normalized instantaneous power of the system gives the best transmit power efficiency. The CDF is set to be $10^{-2}$ in the simulation, and the performance of STBC+PI (Fig. 2.11) equivalent to $\theta = 0$ is also shown in the figure. From Fig. 2.11, when $\theta$ is 0, the case of TX2 shows the better performance compared to that of TX1 as with Fig. 2.11. On the other hand, the performance relationship between TX1 and TX2 is switched on the basis of Eq. 2.7 in the case of $\theta = \pi$. However, the performances of $\theta = \pi/2$ suppresses the envelope fluctuation between the transmit antennas compared to the case of STBC+PI and decreases the deviation of the normalized instantaneous power about 10 dB. As a results, the phase rotation $\theta = \pi/2$ yields the best transmit power efficiency of the entire system when the proposed phase rotated transmit diversity is applied.

### 2.2.2 BER Performance

In this subsection, we evaluate the bit error ration (BER) performance of the proposed system. Since we are considering a narrow-band system in this section, the simulation was conducted a case of an independent and identically distributed 1-path Rayleigh fading channel. Table 2.2 shows the simulation parameters. In the simulation, we assumed that the synchronization at receiver is ideal. A frame consists of ten blocks, where each block

consists of a CP with eight samples and a data section with eight symbols. In addition, based on the results of Fig. 2.11, we evaluated the performance in the case of $\theta = \pi/2$ for this simulation.

Figure 2.12 plots BER performance versus the averaged $E_b/N_0$ under the different number of the averaged symbol in the proposed pilot-less channel estimation scheme. In the simulation, the maximum Doppler frequency normalized by FSK sample $f_dT_s$ is 0.25 $\%$. For the purpose of the comparison, the performance inserting the pilot blocks at the beginning and end of each frame as the conventional case is also shown in the figure. In the case, after averaging the estimated channel values at each pilot blocks, we obtain an estimated channel value at each sample by interpolating between pilot blocks. Moreover, when the conventional case is applied, a frame consists of twelve blocks due to inserting two pilot blocks. In addition, we evaluate the cases of ideal channel and without interpolation, that is, the averaged channel value at initial sample of FSK symbol is used for all samples in FSK symbol. As seen from Fig. 2.12, the BER performances of the proposed scheme are better than that of the conventional case at any number of averaging symbols. In the conventional case, the estimated channel values in the data blocks are obtained by applying 1st-order Lagrange interpolation between pilot blocks placed at the beginning and end of the frame. Therefore, the performance of the conventional scheme degrades owing to the incapability of following the channel fluctuation. As seen from Fig. 2.12, although the uncoded BER performance of the proposed scheme without the averaging, namely, $P = 1$, shows an error floor due to the effect of noise on the channel estimation at low $E_b/N_0$, the performance improves as the number of averaging symbols increases. Moreover, the case without the interpolation shows almost the same performance as that with interpolation. In this simulation, since channel fluctuation is relatively small in low-speed environment such as $f_dT_s = 0.25\%$, the proposed scheme follows the channel fluctuation without applying 1st-order Lagrange interpolation.

### 2.2.3 BER performance at different Doppler frequency

Figure 2.13 shows the uncoded BER performance of the propose scheme at different normalized Doppler frequencies $f_dT_s$. Here, the simulation environments is same as Tab. 2.2, and the average $E_b/N_0$ is 15 dB. As shown in Fig. 2.13, the proposed channel estimation with the averaging and the interpolation shows better performance irrespective of $f_dT_s$, indicating it advantage for high-speed movement. The proposed scheme performs its estimation by using the initial sample of each FSK symbol instead of a pilot symbol, and the effect of channel fluctuations on the FSK symbols is relatively small because the FSK symbols are short. Moreover, the estimated channel responses are obtained by the Lagrange interpolation. Then, the proposed scheme with averaging and the interpolation makes performs better at any $f_dT_s$ while maintaining the transmission rate. In the proposed scheme, although the performance with $P = 5$ is the best in a low $f_dT_s$ case, that with $P = 3$ shows the best performance in the region of $f_dT_s \leq 3\%$. The noise influence on the channel estimation is suppressed by applying the averaging. However, when the number of averaged symbols is large, the number of symbols at timely separated from the estimating symbol

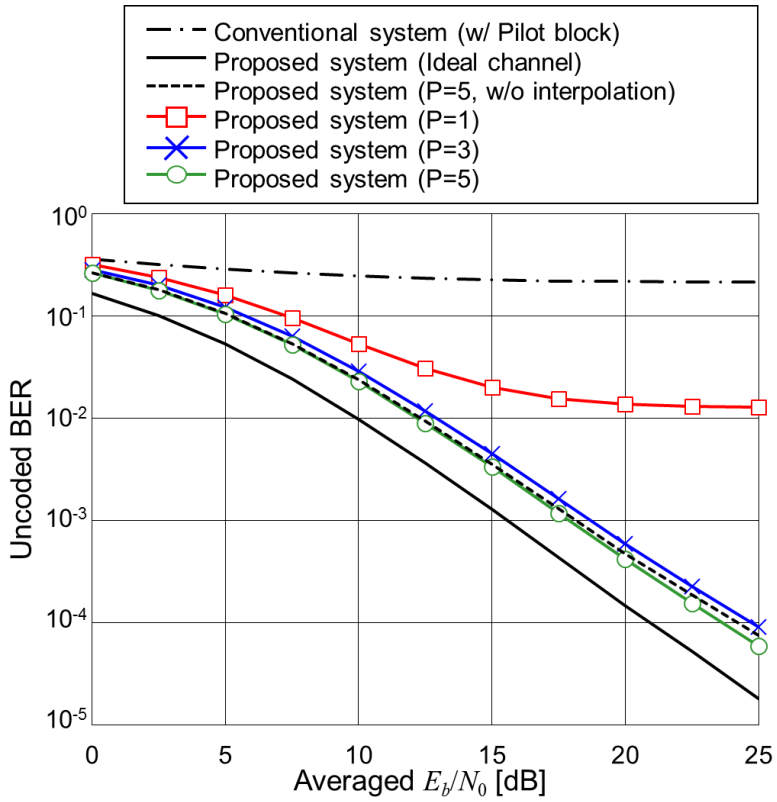


(a) Uncoded BER

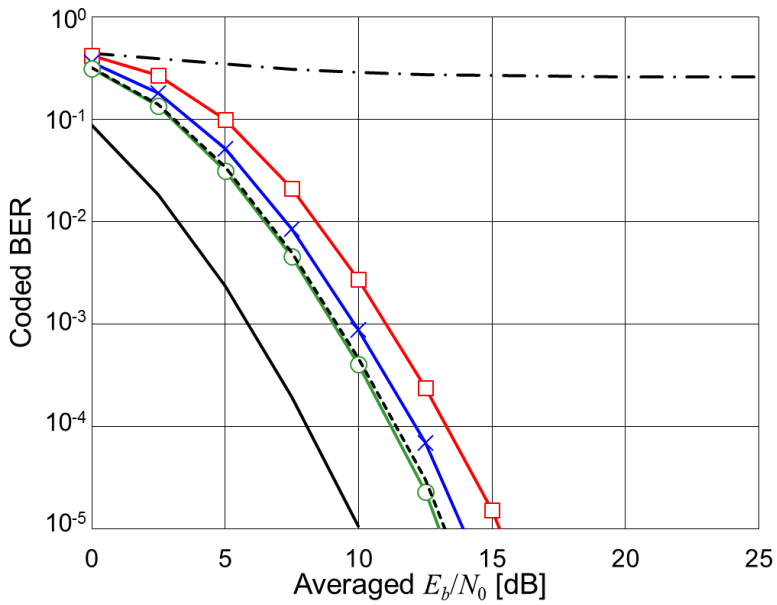


(b) Coded BER

Figure 2.12: BER performance ($f_d T_s = 0.25\%$, $\theta = \pi/2$).

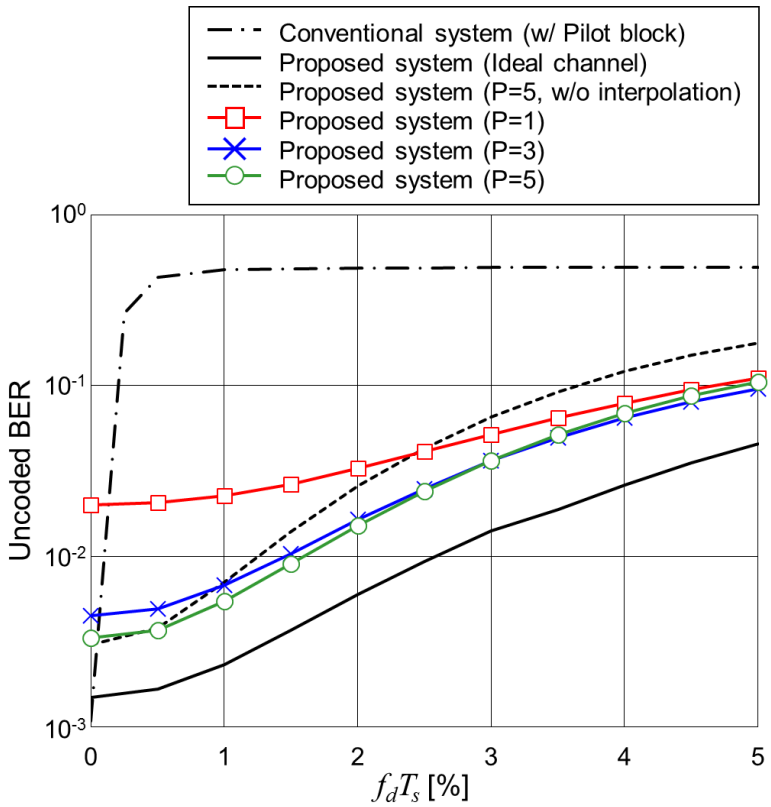


Figure 2.13: BER performance by changing $f_dT_s$ (Averaged $E_b/N_0$=15dB).

increases. As a result, the proposed scheme with $P = 5$ reduces the performance in the large $f_dT_s$ case as the channel fluctuation between the FSK symbols is large.

Therefore, the proposed scheme improve the transmit power efficiency of 10 dB and achieves long-range wireless transmission with high reliability even in the event of high-speed movement.

## 2.3 Conclusions

In this chapter, the author proposed a pilot-less narrow-band coherent FSK system applying phase rotated transmit diversity to achieve long-range mobile wireless communication with high reliability. The phase rotated transmit diversity scheme reduces the phase discontinuity between space-time coded FSK symbols by adding a phase rotation, and therefore suppresses the envelope fluctuation. Furthermore, the proposed system estimates the channel parameters without inserting known pilot symbols by utilizing the fact that FSK is characterised by the initial phase being uniquely determined. Computer simulations have confirmed that the proposed scheme improves the transmit power efficiency by about 10

dB compared to conventional STBC and even improves the performance in the event of high-speed movement.

# Chapter 3

# Two-dimensional Diversity Approach by serially concatenating SP and modified PN-DSTBC

In this chapter, the author proposes an alternative two-dimensional diversity approach concatenated with the SP and modified PN-DSTBC to increase the communication capacity and further maintain the transmit distance.

## 3.1 Power Normalized-Differential Space-Time Block Coding scheme

As stated in Sect. 2.1.1, although STBC achieves the full diversity gain, it needs the channel response to decode signals. Hence, the performance of STBC is seriously degraded due to the fading in the high-speed moving environments. On the other hand, DSTBC is able to realize the transmit diversity without the knowledge of the channels thanks to the differential encoding [31].

First, at the transmitter, a differential encoding is operated by using differential-coded signal one STBC block before, and we have

$$\begin{bmatrix} u_{k,1} \\ u_{k,2} \end{bmatrix} = \begin{bmatrix} s_{k,1} & -s_{k,2} \\ s*_{k,2} & s^*_{k,1} \end{bmatrix} \begin{bmatrix} u_{k-1,1} \\ u_{k-1,2} \end{bmatrix}, \tag{3.1}$$

where $s_{k,i}$ denotes a modulated signal, $u_{k,i}$ denotes the differential coded signal, $i$ is a symbol index $(i = 1, 2)$, $k$ is a block index for STBC coding $(k = 1, 2)$. In the differential encoding, when non-constant envelope modulation scheme, such as QAM, is applied, the envelope fluctuation increases as the number of STBC block increasing. As a result, it

causes the performance degradation due to a non-linear distortion. Therefore, in order to suppress the influence of the fluctuation, a normalization is applied to the differential encoding by using an amplitude of the encoded signal one STBC block before [32, 33]. The differential encoded signal with power normalization is given by

$$\begin{bmatrix} u_{k,1} \\ u_{k,2} \end{bmatrix} = \frac{1}{\sqrt{|u_{k-1,1}|^2 + |u_{k-1,2}|^2}} \begin{bmatrix} s_{k,1} & -s_{k,2} \\ s^*_{k,2} & s^*_{k,1} \end{bmatrix} \begin{bmatrix} u_{k-1,1} \\ u_{k-1,2} \end{bmatrix}. \tag{3.2}$$

After that, STBC is applied to the encoded signal given by (3.2), and we have

$$\begin{bmatrix} x^{(1)}_{k,1} & x^{(1)}_{k,2} \\ x^{(2)}_{k,1} & x^{(2)}_{k,2} \end{bmatrix} = \begin{bmatrix} u_{k,1} & -u^*_{k,2} \\ u_{k,2} & u^*_{k,1} \end{bmatrix}. \tag{3.3}$$

Here, $x^{(m)}_{k,i}$ indicates a transmit signal and $m$ is the index of the transmit antenna $(m = 1, 2)$.

A received signal is given by

$$\begin{bmatrix} r_{k,1} \\ r_{k,2} \end{bmatrix} = \begin{bmatrix} x^{(1)}_{k,1} & x^{(1)}_{k,2} \\ x^{(2)}_{k,1} & x^{(2)}_{k,2} \end{bmatrix} \begin{bmatrix} h^{(1)} \\ h^{(2)} \end{bmatrix} + \begin{bmatrix} n_{k,1} \\ n_{k,2} \end{bmatrix}, \tag{3.4}$$

where $h^{(m)}$ indicates a channel between nature between $m$-th transmit antenna and the received antenna and $n_{k,i}$ denotes an AWGN component. Considering the power normalization shown in (3.2), the DSTBC decoded signal is given by

$$\begin{bmatrix} \tilde{s}_{k,1} \\ \tilde{s}_{k,2} \end{bmatrix} = \frac{1}{\sqrt{|h^{(1)}|^2 + |h^{(2)}|^2}} \frac{1}{\sqrt{|r_{k-1,1}|^2 + |r_{k-1,2}|^2}} \begin{bmatrix} r^*_{k-1,1} & r_{k-1,2} \\ -r^*_{k-1,2} & r_{k-1,1} \end{bmatrix} \begin{bmatrix} r_{k,1} \\ r_{k,2} \end{bmatrix}. \tag{3.5}$$

As shown in the above equation, the PN-DSTBC decoder needs to an information about the amplitude of channels although the DSTBC decoder does not need that [31]. However, since inserting a start symbol which is known between the transmitter and the receiver is necessarily for the differential encoding, the receiver obtains the channel response by using the start symbol. Furthermore, the DSTBC decoder uses the amplitude of the channels only as shown in (3.5). Then, PN-DSTBC is effective technique for reducing the severe effects of oscillator phase noise in EHF band.

## 3.2 Transmitter of PN-DSTBC with Spectral Precoding

Let us assume a $2\times1$ multi-input single-output (MISO) system model with multiple transmit carriers. In our study, the narrowband multicarrier system, such as orthogonal frequency division multiplexing (OFDM), is applied as shown in Fig. 3.1, and the diversity techniques are applied to each subcarrier symbol. Therefore, in the following discussion, we focus on the subcarriers. Furthermore, we assume that the subcarrier channel is the flat fading [55] and the frequency selectivity exists between the subcarrier channels. Here,

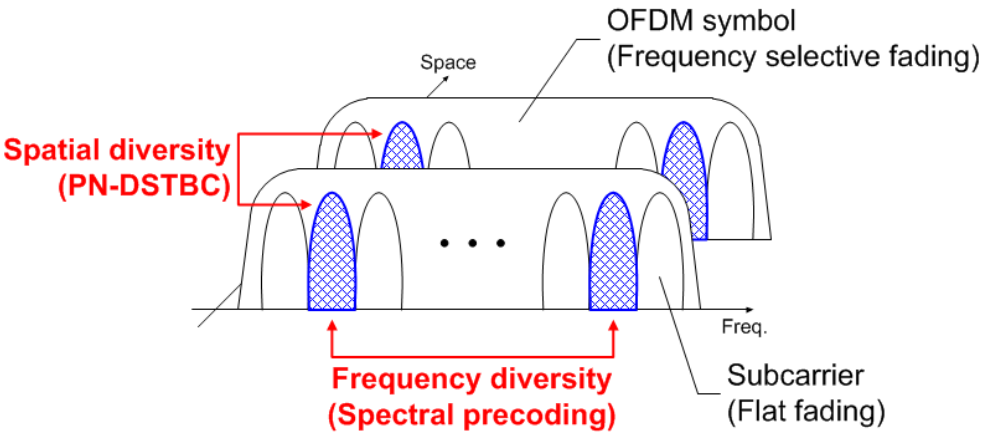


Figure 3.1: Transmit frequency bands (two carriers case).

$s_{k,i,j}$ denotes a modulated signal and $j$ is a transmission carrier index ($j$=1, 2). First, at the transmitter, $s_{k,i,j}$ is spectrally precoded by multiplying a $2 \times 2$ precoding matrix $\boldsymbol{\phi}$, and we have

$$\begin{bmatrix} z_{k,i,1} \\ z_{k,i,2} \end{bmatrix} = \boldsymbol{\phi} \begin{bmatrix} s_{k,i,1} \\ s_{k,i,2} \end{bmatrix}. \tag{3.6}$$

The precoding matrix is designed with a parameter $\alpha$ $(0.5 \leq \alpha \leq 1)$ which defined a multiplexing power ratio of two signals and is given by

$$\boldsymbol{\phi} = \begin{bmatrix} \sqrt{\alpha} & -\sqrt{1-\alpha} \\ \sqrt{1-\alpha} & \sqrt{\alpha} \end{bmatrix}. \tag{3.7}$$

After spectral precoding, DSTBC coding with power normalization, i.e. PN-DSTBC, is applied to the precoded signal $z_{k,i,j}$ taking into account suppressing the fluctuation in amplitude especially for the case of non-constant envelope modulations such as QAM. As stated in Sect. 3.1, in PN-DSTBC coding, $z_{k,i,j}$ is differentially encoded with power normalization and STBC coding. Then, an encoded signal $\boldsymbol{u}_{k,j} = [u_{k,1,j} \quad u_{k,2,j}]^T$ is given by

$$\mathcal{Q}(\boldsymbol{u}_{k,j}) = \mathcal{Q}(\boldsymbol{z}_{k,j}) \frac{\mathcal{Q}(\boldsymbol{u}_{k-1,j})}{||\boldsymbol{u}_{k-1,j}||}. \tag{3.8}$$

Here, $\mathcal{Q}(\boldsymbol{x})$ denotes a quaternion with complex matrix representation of $\boldsymbol{x}$ and is given by

$$\mathcal{Q}(\boldsymbol{x}) = \begin{bmatrix} x_1 & -x_2^* \\ x_2 & x_1^* \end{bmatrix}, \tag{3.9}$$

where

$$\mathcal{Q}^H(\boldsymbol{x})\mathcal{Q}(\boldsymbol{x}) = \mathcal{Q}(\boldsymbol{x})\mathcal{Q}^H(\boldsymbol{x}) = ||\boldsymbol{x}||^2 \boldsymbol{I}_2, \tag{3.10}$$

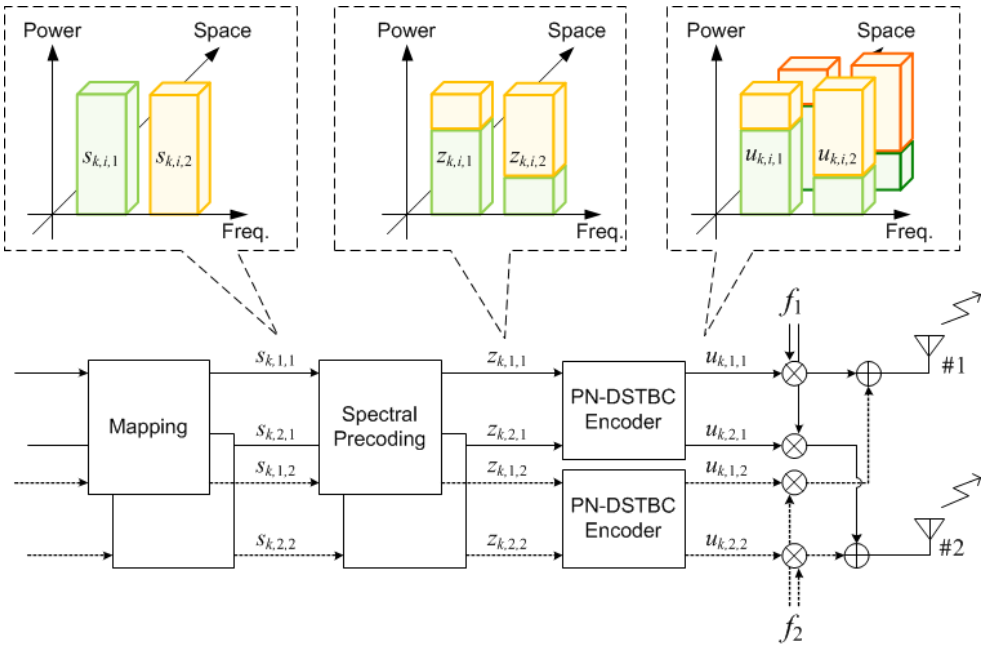


Figure 3.2: System model (Transmitter, two carriers case).

and

$$\mathcal{Q}(\boldsymbol{x}) \begin{bmatrix} 1 \\ 0 \end{bmatrix} = \boldsymbol{x} = [x_1 \; x_2]^T. \tag{3.11}$$

Here, $(\cdot)^H$ denotes the Hermitian transpose.

Figure 3.2 shows the system model of the transmitter. As shown in Fig. 3.2, the information signal $z_{k,i,j}$, which is precoded two modulated signal at a ratio given by the precoding matrix, is applied PN-DSTBC over two transmit antennas. Then, the encoded signal $u_{k,i,j}$ is transmitted at carrier $f_j$ from the two transmit antennas.

## 3.3 Receiver of PN-DSTBC with Spectral Precoding

A received signal can be represented by

$$\mathcal{Q}(\boldsymbol{r}_{k,j}) = \mathcal{Q}(\boldsymbol{u}_{k,j})\mathcal{Q}(\boldsymbol{h}_j) + \mathcal{Q}(\boldsymbol{\eta}_{k,j}). \tag{3.12}$$

Here, $\boldsymbol{h}_j = [h_j^{(1)} \; h_j^{(2)}]^T$ and $h_j^{(m)}$ denotes a channel nature between $m$-th transmit antenna and the received antenna at carrier $f_j$, and $\boldsymbol{\eta}_{k,j}$ indicates an AWGN component. Note that $\eta_{k,i,j}$ obeys complex Gaussian distribution of which mean and variance are 0 and $2N_0$, respectively, regardless of the carrier and the time.

Figure 3.3 shows the system model of the receiver. As shown in Fig. 3.3, even if there is a severe selectivity in channels, two information signals at each carrier can be decoded

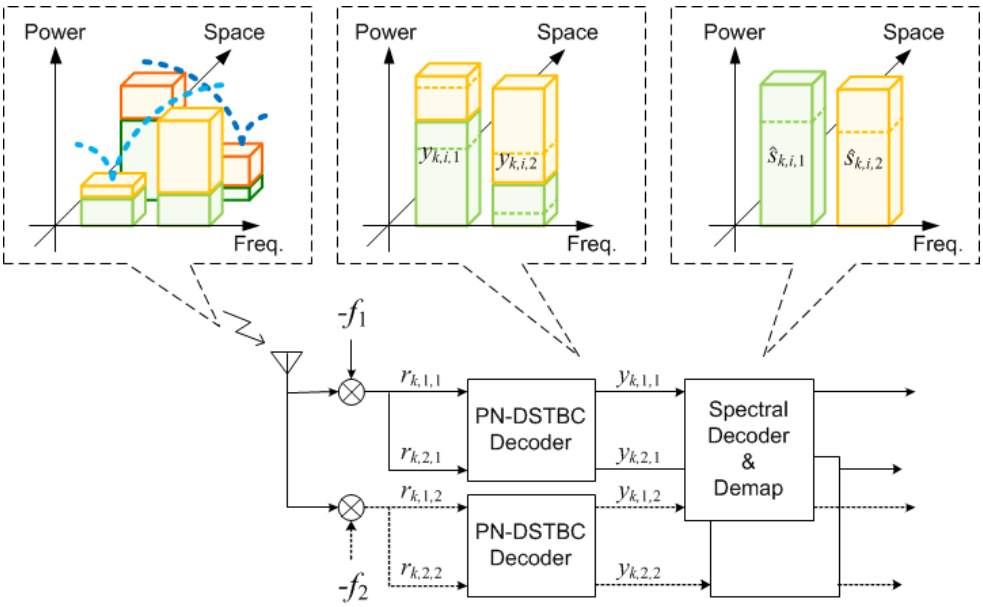


Figure 3.3: System model (Receiver, two carriers case).

at the receiver with the frequency diversity and the spatial diversity. Hereinafter, we will use the term "SP-PN-DSTBC" to refer to the concatenation of the spectral precoding and PN-DSTBC as shown in Fig. 3.2 and 3.3.

### 3.3.1 PN-DSTBC Decoder

First, at the receiver, PN-DSTBC decoder output, using the received signal $\boldsymbol{r}_{k,j}$, is expressed by the following equation:

$$\begin{aligned}\mathcal{Q}(\boldsymbol{y}_{k,j}) &= \mathcal{Q}(\boldsymbol{r}_{k,j})\mathcal{Q}^H(\boldsymbol{r}_{k-1,j}) \\ &= (\mathcal{Q}(\boldsymbol{u}_{k,j})\mathcal{Q}(\boldsymbol{h}_j) + \mathcal{Q}(\boldsymbol{\eta}_{k,j}))(\mathcal{Q}(\boldsymbol{u}_{k-1,j})\mathcal{Q}(\boldsymbol{h}_j) + \mathcal{Q}(\boldsymbol{\eta}_{k-1,j}))^H \\ &= ||\boldsymbol{h}_j||^2\mathcal{Q}(\boldsymbol{u}_{k,j})\mathcal{Q}^H(\boldsymbol{u}_{k-1,j}) + \mathcal{Q}(\boldsymbol{\eta}^{(1)}) \\ &= ||\boldsymbol{h}_j||^2||\boldsymbol{z}_{k-1,j}||\mathcal{Q}^T(\boldsymbol{z}_{k,j}) + \mathcal{Q}(\boldsymbol{\eta}^{(1)}). \end{aligned} \tag{3.13}$$

Here, $||\boldsymbol{h}_j||^2||\boldsymbol{z}_{k-1,j}||$ means the equivalent channel at the PN-DSTBC decoder. $\mathcal{Q}(\boldsymbol{\eta}^{(1)})$ denotes the equivalent noise and is given by

$$\mathcal{Q}(\boldsymbol{\eta}^{(1)}) = \mathcal{Q}(\boldsymbol{u}_{k,j})\mathcal{Q}(\boldsymbol{h}_j)\mathcal{Q}^H(\boldsymbol{\eta}_{k-1,j}) + \mathcal{Q}(\boldsymbol{\eta}_{k-1,j})\mathcal{Q}^H(\boldsymbol{r}_{k-1,j}), \tag{3.14}$$

where $\mathcal{Q}(\boldsymbol{\eta}^{(1)})[1\ 0]^T$ has an instantaneous variance $2N_0(||\boldsymbol{z}_{k,j}||^2||\boldsymbol{h}_j||^2 + ||\boldsymbol{r}_{k-1,j}||^2)$. The equivalent noise variance changes due to applying PN-DSTBC decoder, and it varies on the carrier. As shown in Fig. 3.3, the observation of the spectral decoder are coming from different PN-DSTBC decoder blocks which generates different noise variances. Therefore,

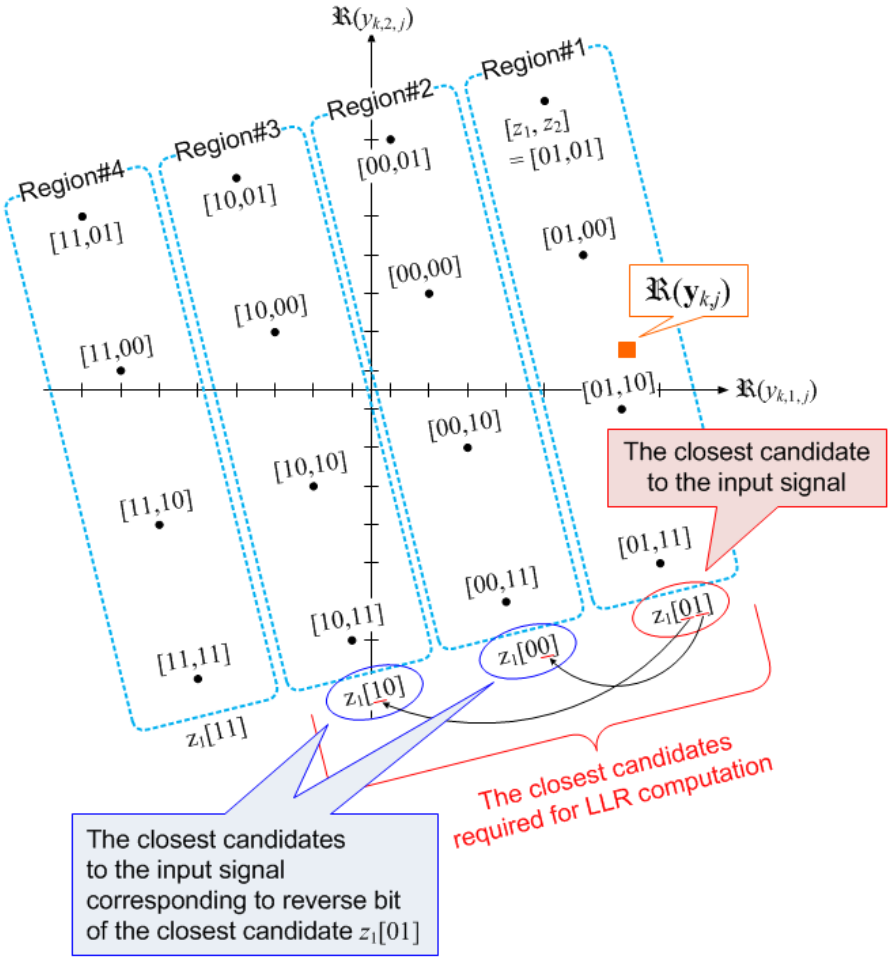


Figure 3.4: Constellation of the symbol replica candidates (16QAM, two carriers case).

the spectral decoder needs to consider the imbalance of the equivalent noise variances of PN-DSTBC decoder outputs.

### 3.3.2 Spectral Decoder

In this system, the decoded signal $z_{k,i,j}$ is spectrally decoding using Maximum Likelihood Detection (MLD) after PN-DSTBC decoder. In the case of $2^{2N}$-QAM ($N$ is an integer of 2 or more) and two transmit carriers, we need $2^{2N} \times 2^{2N} = 2^{4N}$ symbol replica candidates to decode a symbol vector in the exhaustive MLD. For this reason, the number of symbol candidates makes it difficult to implement the spectral decoder.

Hence, the decoding method shown in [56] (hereinafter referred to as "equivalent MLD") reduces the number of symbol candidates by splitting a encoded complex signal into a real and an imaginary components and sequentially processing predetermination and

Table 3.1: Number of symbol replica candidates (two carriers case)

| Modulation scheme ($2^{2N}$-QAM) | Exhaustive MLD ($2^{4N}$) | Equivalent MLD ($2^{N+2}$) | Simplified MLD ($4(N+1)$) |
|---|---|---|---|
| 16QAM | 256 | 16 | 12 |
| 64QAM | 4096 | 32 | 16 |
| 256QAM | 65536 | 64 | 20 |
| 1024QAM | 1048576 | 128 | 24 |

estimation of symbols. Moreover, a Log-Likelihood Ratio (LLR) value is calculated by the probability of "0" and that of "1", which can be approximately computed by the squared Euclidean distance between the input signal of the spectral decoder and its closest candidate for each bit [57]. Therefore, we can achieve more reduction in the number of symbol candidates by excluding the candidates which are far from the input signal for LLR computation, namely, each of real and imaginary components can be predetermined to $(N+1)$ candidates composed of the closest candidate and $N$ bitwise candidates corresponding to reverse bits. As shown in Fig. 3.4, when the real number component of the input signal is in region $\#1$, the symbol replica candidate $z_1 = [01]$ is selected as the closest candidate to the input signal. In addition to this, the symbol candidates whose value is corresponding to the reverse bit, that is, $z_1 = [00]$, $[10]$, and $[11]$, are needed to calculate LLR values at each bit. However, since $z_1 = [11]$ is further from the input signal than the other candidates, we pick up only the candidates $z_1 = [00],\ [10]$ as the closest candidates with reverse bit of $z_1 = [01]$ to reduce the number of symbol replica candidates. Therefore, the decoding method (hereinafter referred to as "simplified MLD") needs just $2\times2\times(N+1) = 4(N+1)$ possible candidates to demultiplex each symbol vector. It does not cause the degradation in the decoding because the simplified MLD reduce the number of the candidates without any approximation. As shown in Tab. 3.1, when the modulation level is high, the simplified MLD reduces the number of symbol candidates significantly.

Since the simplified MLD assumes that the input noise is Gaussian and its distribution is identical irrespective of the transmit carrier to reduce the decoding complexity, the frequency diversity gain of the spectral precoding decreases due to the imbalance of the equivalent noise variances at PN-DSTBC decoder. Moreover, since the number of candidates increases in the case where the modulation level is high and/or the number of carriers is large, the equivalent noise imbalance has tremendous impact on the decoding performance.

Hence, in the next section, we propose the equalized PN-DSTBC decoder which provides the uniform noise variances to obtain the frequency diversity gain of the spectral precoding.

## 3.4 Equalization: Equivalent Channel Approximation

As mentioned in Sect. 3.3.2, the noise imbalance at PN-DSTBC decoding causes the performance degradation. In order to mitigate the effect, we propose a modified approach which makes an approximation of the channel model.

From (3.9) and (3.12), the received signal is rewritten as

$$\begin{aligned}\mathcal{Q}(\boldsymbol{r}_{k,j}) &= \mathcal{Q}(\boldsymbol{z}_{k,j})\frac{\mathcal{Q}(\boldsymbol{r}_{k-1,j}) - \mathcal{Q}(\boldsymbol{\eta}_{k-1,j})}{||\boldsymbol{r}_{k-1,j} - \boldsymbol{\eta}_{k-1,j}||}||\boldsymbol{h}_j|| \\ &= \mathcal{Q}(\boldsymbol{z}_{k,j})\alpha_{k,j}||\boldsymbol{h}_j|| + \mathcal{Q}(\boldsymbol{\eta}_{k,j}),\end{aligned} \tag{3.15}$$

where $\alpha_{k,j}$ is a channel coefficient which is an unimodular random variable independent from $\boldsymbol{\eta}_{k,j}$ and given by

$$\alpha_{k,j} = \frac{\mathcal{Q}(\boldsymbol{r}_{k-1,j}) - \mathcal{Q}(\boldsymbol{\eta}_{k-1.j})}{||\boldsymbol{r}_{k-1,j} - \boldsymbol{\eta}_{k-1,j}||}. \tag{3.16}$$

Here, we make an Gaussian approximation of channel coefficient $\alpha_{k,j}$ with approximation parameters $\beta_1$ and $\beta_2$, and we have

$$\frac{\mathcal{Q}(\boldsymbol{r}_{k-1,j}) - \mathcal{Q}(\boldsymbol{\eta}_{k-1.j})}{||\boldsymbol{r}_{k-1,j} - \boldsymbol{\eta}_{k-1,j}||} \approx \beta_1\frac{\mathcal{Q}(\boldsymbol{r}_{k-1,j})}{||\boldsymbol{r}_{k-1,j}||} + \beta_2\frac{\mathcal{Q}(\boldsymbol{\eta}_{k-1,j})}{||\boldsymbol{r}_{k-1,j}||}. \tag{3.17}$$

Substituting (3.15) into (3.13), we obtain the decoded signal with new channel model and we have

$$\mathcal{Q}(\boldsymbol{y}_{k,j}) = \beta_1\frac{\mathcal{Q}(\boldsymbol{r}_{k-1,j})}{||\boldsymbol{r}_{k-1,j}||}||\boldsymbol{h}_j||\mathcal{Q}^H(\boldsymbol{r}_{k-1,j})\mathcal{Q}(\boldsymbol{z}_{k,j}) + \mathcal{Q}(\boldsymbol{\eta}^{(2)}). \tag{3.18}$$

Hence, the equivalent noise $\mathcal{Q}(\boldsymbol{\eta}^{(2)})$ is given by

$$\mathcal{Q}(\boldsymbol{\eta}^{(2)}) = \beta_2\frac{\mathcal{Q}(\boldsymbol{\eta}_{k-1,j})}{||\boldsymbol{r}_{k-1,j}||}||\boldsymbol{h}_j||\mathcal{Q}^H(\boldsymbol{r}_{k-1,j})\mathcal{Q}(\boldsymbol{z}_{k,j}) + \mathcal{Q}(\boldsymbol{\eta}_{k,j})\mathcal{Q}^H(\boldsymbol{r}_{k-1,j}), \tag{3.19}$$

which leads to a Gaussian noise of variance $2N_0(\beta_2^2||\boldsymbol{h}_j||^2\ ||\boldsymbol{z}_{k,j}||^2 + ||\boldsymbol{r}_{k-1,j}||^2)$. In order to equalize the noise variance, we apply a filtering and we have

$$\begin{aligned}&\frac{\mathcal{Q}(\boldsymbol{y}_{k,j})}{\sqrt{\beta_2^2||\boldsymbol{h}_j||^2||\boldsymbol{z}_{k,j}||^2 + ||\boldsymbol{r}_{k-1,j}||^2}} \\ &= \frac{\beta_1||\boldsymbol{h}_j||||\boldsymbol{r}_{k-1,j}||}{\sqrt{\beta_2^2||\boldsymbol{h}_j||^2||\boldsymbol{z}_{k,j}||^2 + ||\boldsymbol{r}_{k-1,j}||^2}}\mathcal{Q}(\boldsymbol{z}_{k,j}) + \mathcal{Q}(\boldsymbol{\eta}^{(3)}).\end{aligned} \tag{3.20}$$

Here, the approximated variance of the equivalent noise $\mathcal{Q}(\boldsymbol{\eta}^{(3)})$ is $2N_0$. However, it is difficult to know $||\boldsymbol{z}_{k,j}||^2$ at the receiver side. Thus, we make an approximation $||\boldsymbol{z}_{k,j}||^2||\boldsymbol{h}_j||^2 \approx ||\boldsymbol{r}_{k,j}||^2$ to (3.20) and we have

$$\frac{\beta_1||\boldsymbol{h}_j||||\boldsymbol{r}_{k-1,j}||}{\sqrt{\beta_2^2||\boldsymbol{r}_{k,j}||^2 + ||\boldsymbol{r}_{k-1,j}||^2}}\mathcal{Q}(\boldsymbol{z}_{k,j}) + \mathcal{Q}(\boldsymbol{\eta}^{(4)}). \tag{3.21}$$

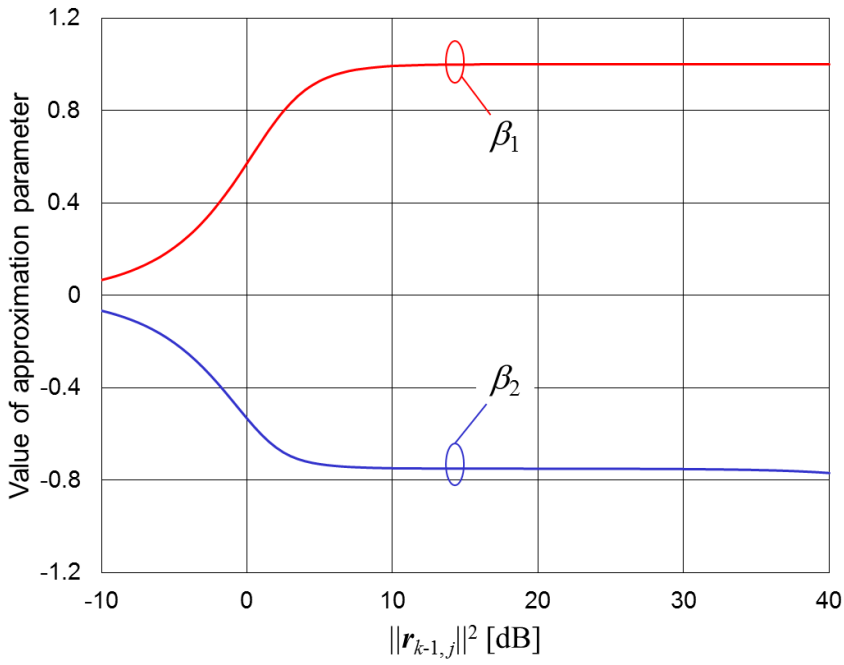


Figure 3.5: Approximation parameters $\beta_1, \beta_2$ by changing $||\boldsymbol{r}_{k-1,j}||^2$.

As shown in the above equation, the filtering coefficient only depends on the received signal $||\boldsymbol{r}_{k,j}||^2$ and $||\boldsymbol{r}_{k-1,j}||^2$.

Next, we optimize the approximation parameters $\beta_1$ and $\beta_2$ to fit the Gaussian distribution by minimizing the mean squared error:

$$f(\beta_1,\ \beta_2) = E\left[\left|\left|\alpha_{k,j} - \beta_1 \frac{\mathcal{Q}(\boldsymbol{r}_{k-1,j})}{||\boldsymbol{r}_{k-1,j}||} - \beta_2 \frac{\mathcal{Q}(\boldsymbol{\eta}_{k-1,j})}{||\boldsymbol{r}_{k-1,j}||}\right|\right|^2\right], \tag{3.22}$$

where $E[\cdot]$ denotes the ensemble average. The singular points of $f(\beta_1,\ \beta_2)$ are obtained for $df(\beta_1,\ \beta_2)/d\beta_1 = 0$ and $df(\beta_1,\ \beta_2)/d\beta_2 = 0$. Thus, we obtain

$$\beta_1 = E\left[\Re\left(\frac{\mathcal{Q}(\boldsymbol{r}_k^H)}{||\boldsymbol{r}_{k-1,j}||}\left(\frac{\mathcal{Q}(\boldsymbol{r}_{k-1,j}) - \mathcal{Q}(\boldsymbol{\eta}_{k-1,j})}{||\boldsymbol{r}_{k-1,j} - \boldsymbol{\eta}_{k-1,j}||}\right)\right)\right], \tag{3.23}$$

$$\frac{\beta_2}{||\boldsymbol{r}_{k-1,j}||^2} E[||\boldsymbol{\eta}_{k-1,j}||^2] = \beta_1 - E\left[\frac{||\boldsymbol{r}_{k-1,j} - \boldsymbol{\eta}_{k-1,j}||}{||\boldsymbol{r}_{k-1,j}||}\right]. \tag{3.24}$$

Here, $\Re(\cdot)$ denotes the real number components. As seen from the above equations, the approximation parameters $\beta_1$ and $\beta_2$ are functions of the received signal $\boldsymbol{r}_{k,j}$ and $\boldsymbol{r}_{k-1,j}$ which are scalars. Therefore, it is enough to have an one-dimensional table for the approximation parameters which can be computed in advance.

Figure 3.5 shows the value of the approximation parameters $\beta_1$ and $\beta_2$ versus the power of the received signal $||\boldsymbol{r}_{k-1,j}||^2$. In this simulation, since the noise power is set to be 0dB,

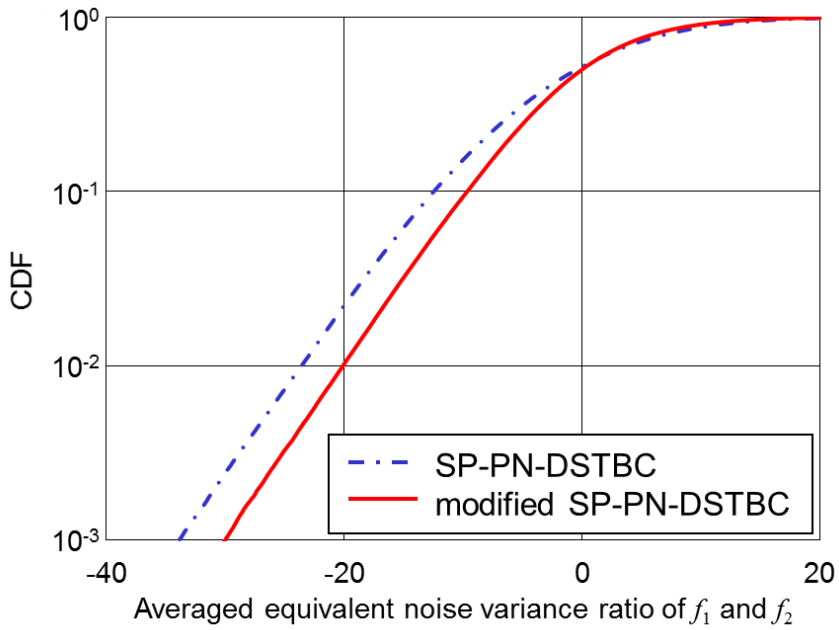


Figure 3.6: CDF performance of averaged equivalent noise ratio of $f_1$ and $f_2$ (two carriers case).

the horizontal axis is equivalent to SNR on the condition that noise variances of two carriers are the same. As shown in Fig. 3.5, we need an look-up table in order to select $\beta_1$ and $\beta_2$ depending on SNR. In the range of $||\boldsymbol{r}_{k,j}||^2 \leq 5$ dB, however, $\beta_1$ and $\beta_2$ converge to 1.0 and -0.75, respectively. Considering that a noise component is dominant error factor in the low SNR region, we expect that the accuracy of the approximation parameters $\beta_1$ and $\beta_2$ is almost negligible. In the following discussion, we adopt $\beta_1 = 1.0$ and $\beta_2 = -0.75$ for simplification. We note that the frequency selectivity in the channel is not relevant to the selection of $\beta_1$ and $\beta_2$, because $\beta_1$ and $\beta_2$ are calculated by using the received signal power $||\boldsymbol{r}_{k,j}||^2$.

We propose the modified SP-PN-DSTBC concatenated with the spectral precoding and the equalized PN-DSTBC to equalize the equivalent noise variances at each of the carriers. Therefore, the decoded signal is given by

$$\mathcal{Q}(\boldsymbol{y}_{k,j}) = \frac{1}{\gamma_{k,j}} \mathcal{Q}(\boldsymbol{r}_{k,j}) \mathcal{Q}(\boldsymbol{r}_{k-1,j})^H, \tag{3.25}$$

where $\gamma_{k,j}$ is a filtering coefficient and is calculated by

$$\gamma_{k,j} = \sqrt{(-0.75)^2 ||\boldsymbol{r}_{k,j}||^2 + ||\boldsymbol{r}_{k-1,j}||^2}. \tag{3.26}$$

The equalized PN-DSTBC decoder provides a new equivalent channel which is input of

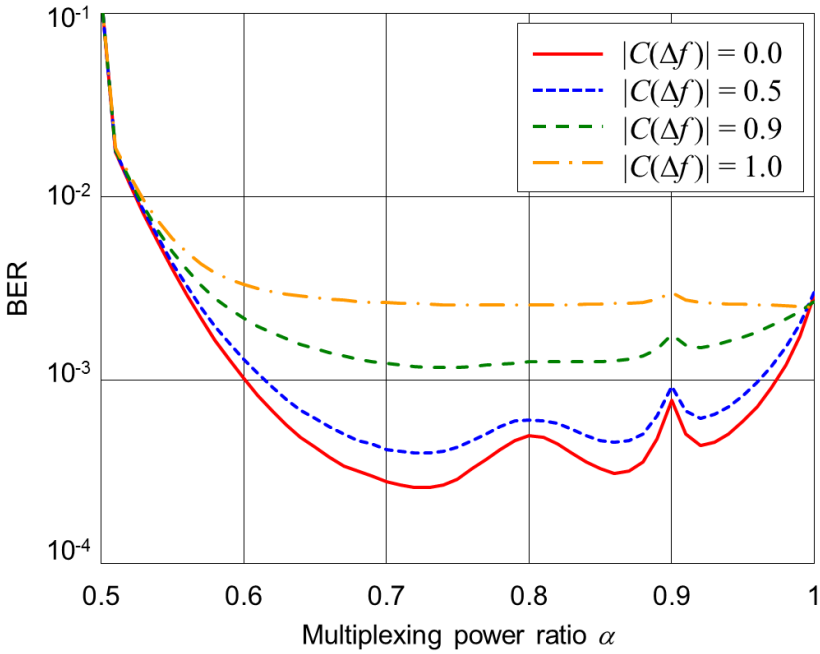


Figure 3.7: BER performance by changing the multiplexing power ratio (two carriers case).

the simplified MLD and it is given by

$$\hat{\boldsymbol{h}}_j = \frac{||\boldsymbol{h}_j||\ ||\boldsymbol{r}_{k-1,j}||}{\gamma_{k,j}}. \tag{3.27}$$

Figure 3.6 shows the cumulative distribution function (CDF) of the averaged equivalent noise variance ratio of $f_1$ and $f_2$ in the case of the modified SP-PN-DSTBC. For comparison, the CDF performance of SP-PN-DSTBC is also shown in this figure. As shown in Fig. 3.6, the filtering coefficient suppresses the noise imbalance between carriers, and the variance of the modified SP-PN-DSTBC is 4 dB at CDF=$10^{-3}$ compared to SP-PN-DSTBC.

## 3.5 Performance Evaluation

Firstly, using computer simulations, we examined the multiplexing power ratio of the precoding matrix $\alpha$ when the frequency correlation coefficient $|C(\Delta f)|$ is changed. Figure 3.7 plots BER performance versus the power ratio in the case where $|C(\Delta f)|$ is 0.0 (Uncorrelated), 0.5, 0.9, and 1.0, Here, the received signal-to-noise power ratio (SNR) is set to 30.0 dB, and modulation scheme is 16QAM. As shown in Fig. 3.7, we obtain the best performance in a region around $\alpha = 0.7236$ which is equivalent to the value given in [30] at any frequency correlation coefficient. Although we do not show explicity the figure in this

Table 3.2: Simulation parameters

| | |
|---|---|
| No. of antennas | TX: 2, RX: 1 |
| TX signal processing | Spectral precoding<br>Equalized PN-DSTBC |
| Frame configuration | Start symbol: 2 symbols<br>Data symbol: 6 symbols |
| No. of transmit carriers | 2 |
| RX signal processing | Simplified MLD |
| Modulation scheme | QPSK, 16QAM, 64QAM |

paper, we also evaluated the cases of quadrature phase shift keying (QPSK) and 64QAM and obtained similar results that $\alpha \simeq 0.7236$ shows good performance. Based on the result, in the following discussion, we evaluate by using $\boldsymbol{\phi}(\alpha = 0.7236)$.

### 3.5.1 Selection of Multiplexing Power Ratio $\alpha$ in the Precoding Matrix

In this subsection, we evaluated the BER performance of the modified SP-PN-DSTBC in the case of i.i.d. Rayleigh fading channel. Table 3.2 shows the simulation parameters. In the simulation, a frame consists of start symbol section and data symbol section with eight blocks, where each block consists of two symbols. In addition, channel gain for each transmit antenna is estimated by using the start symbols. Moreover, the frequency and the spatial correlation is assumed to be uncorrelated. Figure 3.8 plots the BER of the modified SP-PN-DSTBC versus received signal-to-noise power ratio (SNR) in the case where the number of carriers is two. For comparison, the performance of PN-DSTBC only and that of SP-PN-DSTBC are also shown in this figure. Here, PN-DSTBC only means the system applied the identical matrix as the precoding matrix shown in (3.6). As seen from Fig. 3.8, when the modulation level is low such as QPSK and 16QAM, SP-PN-DSTBC improves compared to PN-DSTBC only by concatenating the spectral precoding and PN-DSTBC. However, in the case of 64QAM, the performance degrades compared to that of PN-DSTBC only. It seems that the cause of the performance degradation is the imbalance of the equivalent noise variances at PN-DSTBC decoder output. As mentioned in Sect. 3.3.2, although the equivalent noise at PN-DSTBC decoding is different at each carrier, general decoding schemes such as the simplified MLD adopted in our study are based on an assumption that noise distribution is identical irrespective of the number of carriers. Thus, the simplified MLD is not able to appropriately work for PN-DSTBC decoding outputs resulting in a decrease in frequency diversity gain. On the other hand, the modified SP-PN-DSTBC makes the performance better at any modulation case, and the improved gain is 4 dB at BER=$10^{-4}$ compared to PN-DSTBC only with 64QAM. As shown in Fig. 3.6, the equalized PN-DSTBC decoder generates the uniform noise variance irrespective of the carrier by applying the filtering coefficient. Therefore, the decoding performance of the simplified MLD increases and it

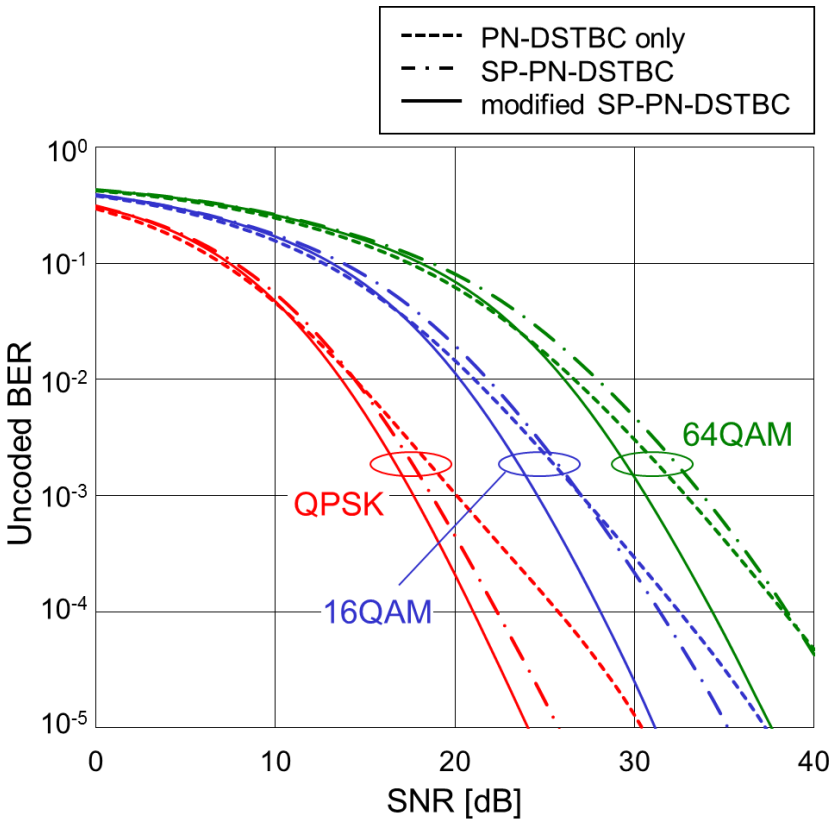


Figure 3.8: BER performance (two carriers case).

results in the potential frequency diversity gain.

### 3.5.2 BER performance on i.i.d. Rayleigh Fading Channel

Figure 3.9 shows the BER performance of the modified SP-PN-DSTBC by changing the frequency correlation coefficient $|C(\Delta f)|$ in two carriers case. Here, the received SNR is set to 22.5 dB in QPSK case, 30.0 dB in 16QAM case, and 37.5 dB in 64QAM case, respectively. The performance of the PN-DSTBC only and that of SP-PN-DSTBC are also shown in the figure. As seen from Fig. 3.9, the performance of PN-DSTBC only is constant independently of the frequency correlation coefficient because PN-DSTBC only is not applied a frequency diversity scheme, namely, the spectral precoding. On the other hand, as the frequency correlation coefficient becomes higher, the performance improvement of the modified SP-PN-DSTBC gradually degrades. The modified SP-PN-DSTBC is applied the spectral precoding in addition to PN-DSTBC. Therefore, the performance of the modified SP-PN-DSTBC varies depending on the frequency correlation coefficient. However, even in the case of the high frequency correlation, such as $|C(\Delta f)| = 0.9$, the performances

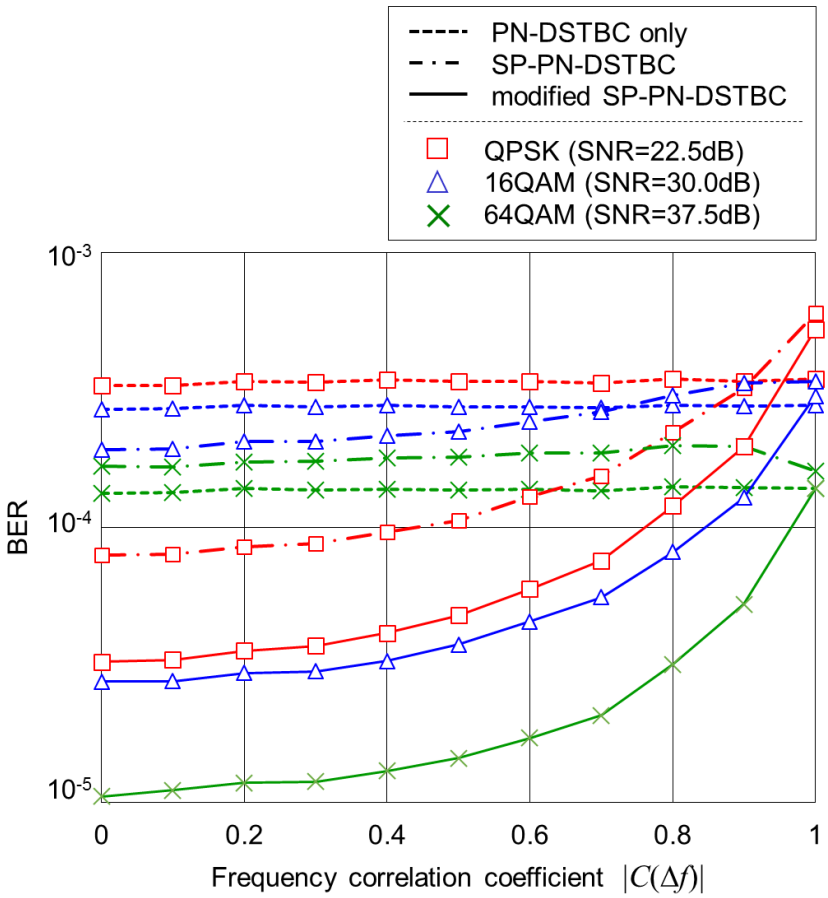


Figure 3.9: BER performance by changing the frequency correlation coefficient (two carriers case).

of the modified SP-PN-DSTBC are better than that of PN-DSTBC only at any modulation schemes.

Figure 3.10 plots the frequency correlation coefficient $|C(\Delta f)|$ versus the frequency separation $\Delta f$MHz for multipath channel models specific in [58]. In Fig. 3.10, TDL-A (tapped delay line model type-A) and TDL-E model non-line-of-sight (NLOS) and LOS channels, respectively. Root mean square (RMS) delay spread $DS_{\text{desired}}$ was set at 18.0ns and 61.0ns as a 39.0GHz normal-delay indoor and urban micro cell prescribed in Table 7.7.3-2 in [58]. As shown in Fig. 3.10, the frequency correlation coefficients of TDL-E case are higher than those of TDL-A case due to a LOS path. However, considering the result in Fig. 3.9 additionally, we can say that the modified SP-PN-DSTBC yields the performance improvement even in the frequency correlation channel case when the frequency separation is larger than 2 MHz in the case of large delay spread.

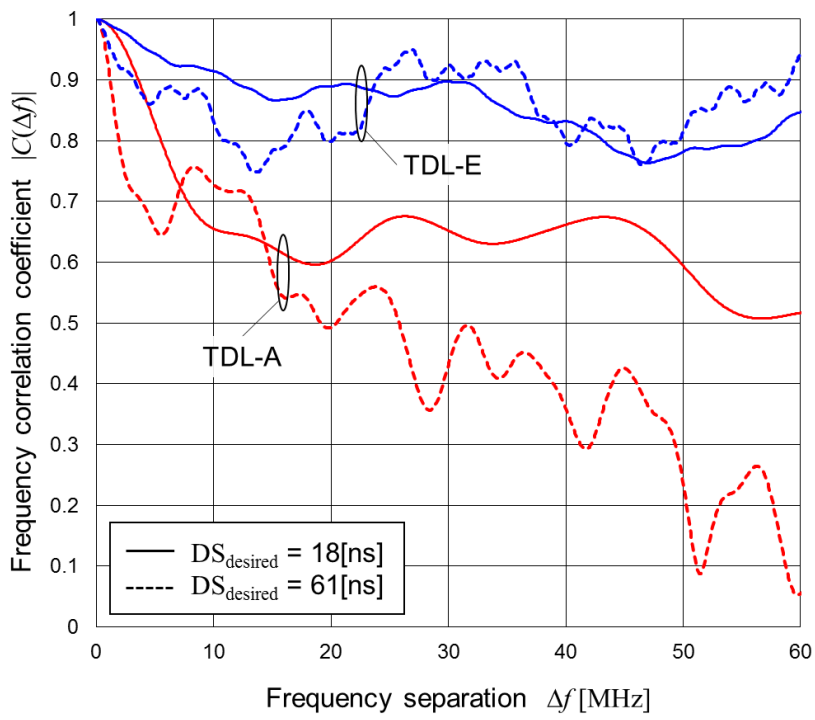


Figure 3.10: Frequency correlation (TDL-A and TDL-E case [58]).

### 3.5.3 BER performance on Frequency Correlated Channel

Figure 3.11 shows the BER performance of the proposed approach by changing the spatial correlation coefficient $|C(\Delta d)|$ in two carriers case. In this simulation, the received SNRs are the same as Fig. 3.9. As seen from Fig. 3.11, the BER performances are degraded due to the spatial correlation. Comparing the BER performance of the modified SP-PN-DSTBC with those of PN-DSTBC only and SP-PN-DSTBC, we also observe that the spatial correlation does not affect the superiority of the proposed scheme. We note that in the case of $|C(\Delta d)| \leq 0.5$, the performance degradation due to the spatial correlation is negligible. As noted in [59, 60], when a spatial separation is larger than $5\lambda$ where $\lambda$ means wavelength, the spatial correlation is sufficiently small, that is, $|C(\Delta d)| \leq 0.5$. Therefore, we can say that the modified SP-PN-DSTBC is effective even in the spatial correlation channel. Therefore, we can say that the superiority of the proposed approach is kept even in the spatially correlated channels.

### 3.5.4 BER performance of the Modified SP-PN-DSTBC with More Than Two Carriers

Figure 3.13 plots the BER performance versus the number of carriers in the case of i.i.d. Rayleigh fading channel. Here, the received SNRs are the same as Fig. 3.9. Fig. 3.12

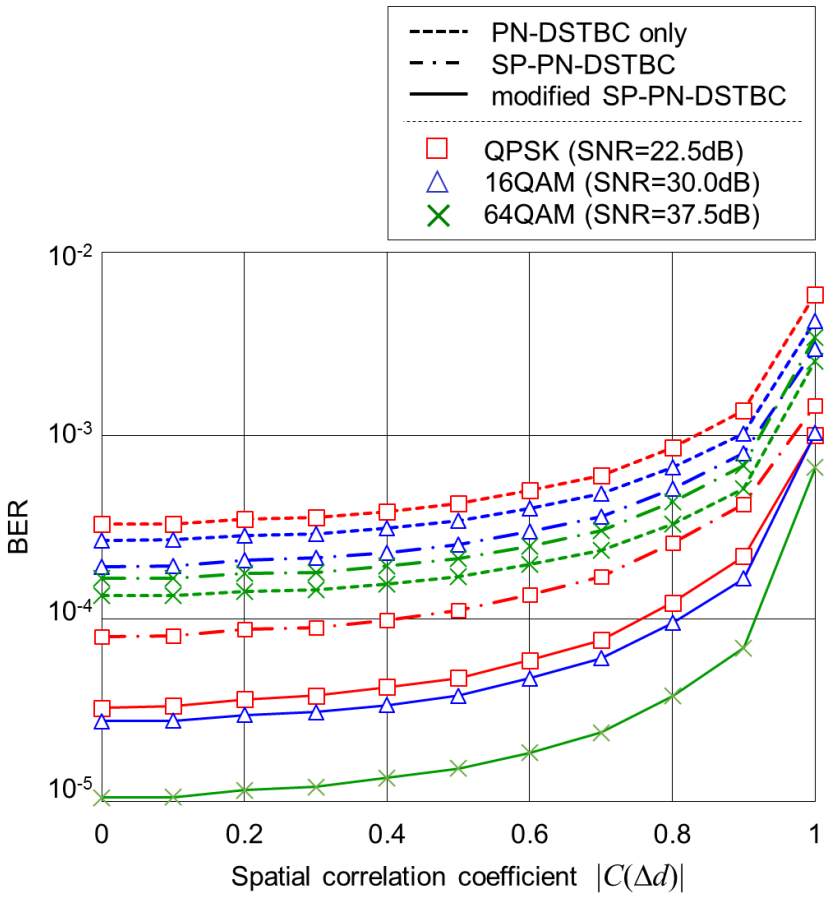


Figure 3.11: BER performance by changing the spatial correlation coefficient (two carriers case).

shows the system model in the case of having $J$ carriers. As shown in Fig. 3.12, when the number of carriers increases, the number of input of the spectral precoding/decoder and the module of PN-DSTBC encoder/decoder increases. In this simulation, the precoding matrix is designed referring to [30] at any number of carriers. In addition to the modified SP-PN-DSTBC, the performance of the PN-DSTBC only and that of SP-PN-DSTBC are also shown in this figure. As shown in Fig. 3.13, in the case of PN-DSTBC only, the BER performances are constant independently of the number of carriers at any modulation schemes. By contrast, thanks to concatenating the spectral precoding and PN-DSTBC, both SP-PN-DSTBC and the modified SP-PN-DSTBC improve the BER performance as the number of carriers increases. Moreover, the performance improvements of the modified SP-PN-DSTBC are greater than those of SP-PN-DSTBC at any modulation schemes because of the equalization of the equivalent noise imbalance between carriers.

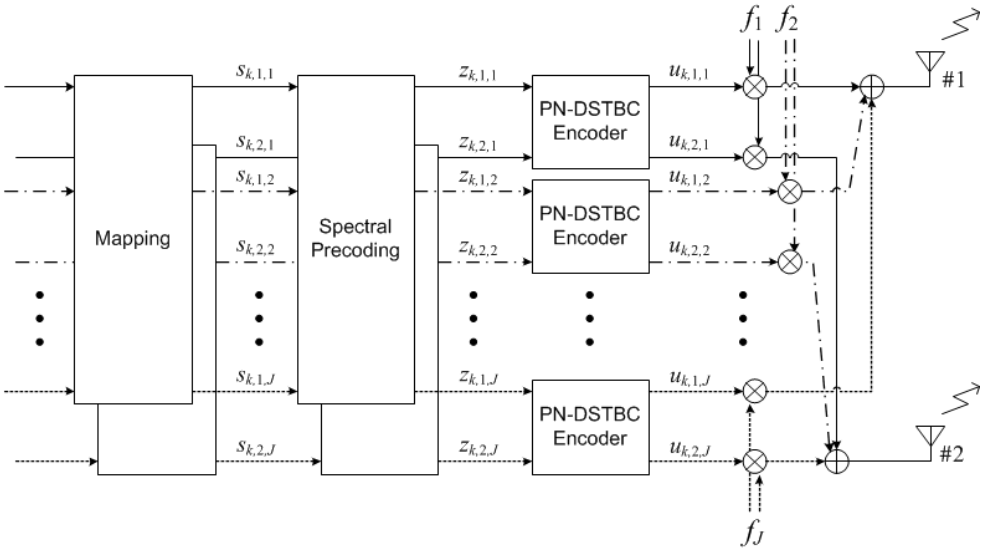


(a) Transmitter

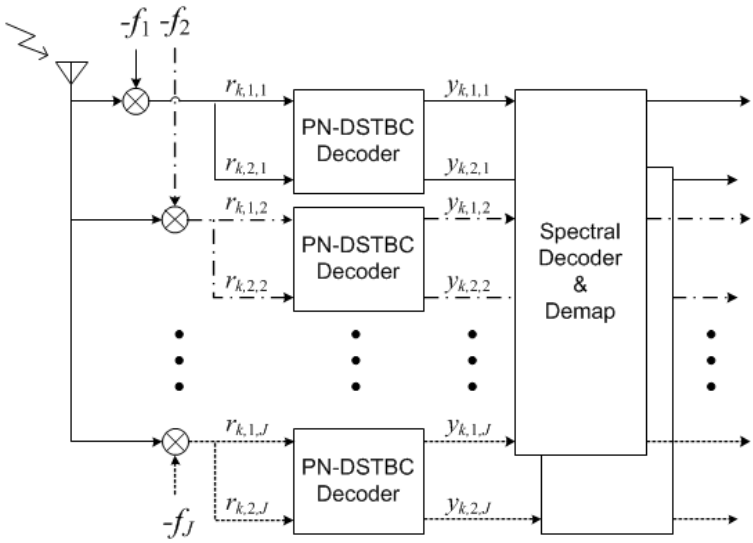


(b) Receiver

Figure 3.12: System model ($J$carriers case).

## 3.6 Conclusions

In this chapter, for satisfying the demands of higher data rate transmission. the author has examined the approach of two-dimensional diversity by serially concatenating spectral precoding and modified PN-DSTBC. Firstly, the author revealed the problem of the equivalent noise imbalance over transmit frequencies. In order to address this issue, the author proposed the modified configuration which compensates the equivalent noise imbalance by

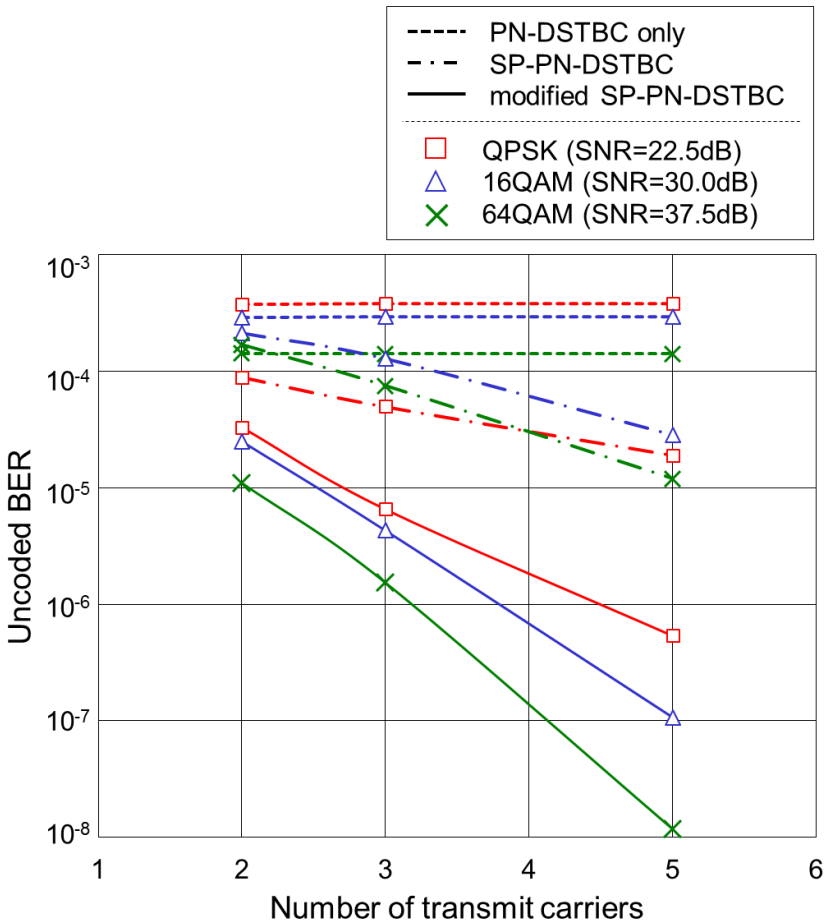


Figure 3.13: BER performance by changing the number of carriers.

applying equalized PN-DSTBC decoder. The computer simulation results clarified that the proposed configuration improves the performance at any modulation level and any number of transmit carriers thanks to the equalization of noise variance imbalance at PN-DSTBC decoder, and the performance improvement is 4 dB at uncoded BER = $10^{-4}$ in the case of 64QAM and two transmit carriers.

# Chapter 4

# Multi-user MIMO System by Using Channel Prediction Techniques

In this chapter, the author examines multi-user MIMO system applying channel prediction techniques and evaluates the performance improvement in cases of Jakes' model and an actual indoor environment.

## 4.1 Multi-user MIMO System

Let us consider a down-link multi-use MIMO system based on a combination of the BD scheme and the E-SDM technique to suppress IUI and IStI as shown in Fig. 4.1. A BS in this system with $N_T$ antennas simultaneously transmits signals to $K$ users (mobile stations (MSs)), and each MS has $N_R$ antennas. The BS needs CSI to determine the transmit weights to use these techniques. Here, we have assumed packet transmission in the time division duplexing (TDD) system shown in Fig. 4.2. Uplink and downlink signals are transmitted with a period of the frame duration $T_f$.

We express transmit signals for the $k$-th MS and the channel matrix for the $k$-th MS at time $t$ as $\boldsymbol{s}_k(t)$ and $\boldsymbol{H}_k(t)$, respectively. The received signal vector at the $k$-th MS is given by

$$\begin{aligned}\boldsymbol{r}_k(t) &= \boldsymbol{H}_k(t)\sum_{m=1}^{K}\boldsymbol{W}_{TX,m}\boldsymbol{s}_m(t) + \boldsymbol{n}_k(t)\\ &= \boldsymbol{H}_k(t)\boldsymbol{W}_{TX,k}\boldsymbol{s}_k(t) + \boldsymbol{H}_k(t)\sum_{m=1,i\neq k}^{K}\boldsymbol{W}_{TX,m}\boldsymbol{s}_m(t) + \boldsymbol{n}_k(t). \qquad (4.1)\end{aligned}$$

In (4.1), the first term is a desired signal for the $k$-th MS, and the second term is interferences from the the other $K-1$ users to the $k$-th MS, namely, IUI. The BS estimates

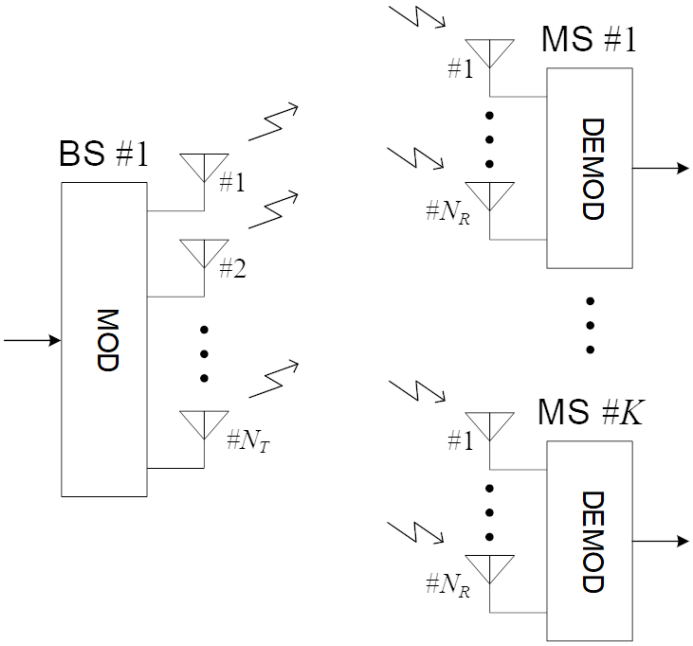


Figure 4.1: Multi-user MIMO system model.

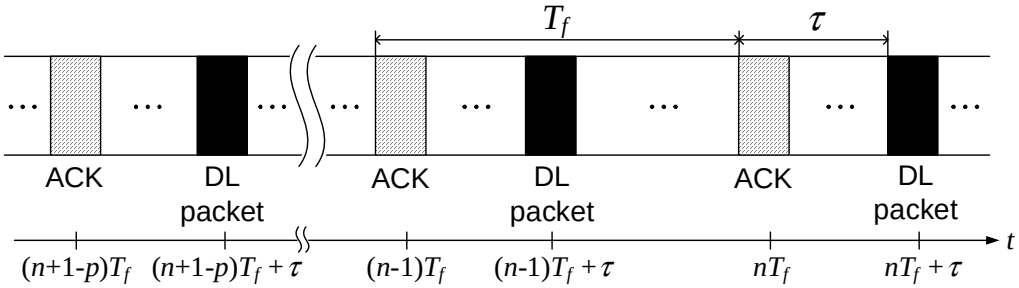


Figure 4.2: TDD transmission frame format.

the channels for the MSs using uplink acknowledge (ACK) packets, and determines the transmit weights based on the BD scheme and the E-SDM technique which are stated in the following section.

### 4.1.1 Block-Diagonalization Scheme

In order to eliminate IUI, in the BD scheme, the $k$-th transmit weight $\boldsymbol{W}_{TX,k}$ must be satisfied as follows;

$$\boldsymbol{H}_m(t)\boldsymbol{W}_{TX,k}(t) = 0 \quad \text{for all } m, k: \quad 1 \leq m \neq k < K. \tag{4.2}$$

Here, $\boldsymbol{H}_m(t)$ denotes a channel matrix of $m$-th MS. The above term implies that columns of $\boldsymbol{W}_{TX,k}(t)$ are in the null space of $\boldsymbol{H}_m(t)$ for $m \neq k$, that is, the transmit weight of the BD scheme are given by a singular value decomposition (SVD) of the channel matrix $\boldsymbol{H}_m(t)$ for all $m \neq k$. It is noted that $\boldsymbol{W}_{TX,k}(t)$ should be nonzero, otherwise, no signal is transmitted. Then, we assume that the number of transmit antennas is larger than the sum of the number of receiver antennas of any $K-1$ users, that is, $N_T > (K-1)N_R$.

The SVD of the channel matrix of other $K-1$ users is given by

$$\hat{\boldsymbol{H}}_k(t) = \hat{\boldsymbol{U}}_k(t)\boldsymbol{\Sigma}(t)(\hat{\boldsymbol{V}}_k(t)\hat{\boldsymbol{V}}_k^0(t))^H, \tag{4.3}$$

where $\hat{\boldsymbol{H}}_k(t)$ is the channel matrix of $K-1$ users, and the rank of $\hat{\boldsymbol{H}}_k(t)$ is $\hat{N}_k$. $\hat{\boldsymbol{V}}_k(t)$ contains the first $\hat{N}_k$ right singular vectors and $\hat{\boldsymbol{V}}_k^0(t)$ contains the last $(N_T - \hat{N}_k)$ right singular vectors of $\hat{\boldsymbol{H}}_k(t)$. The columns in $\hat{\boldsymbol{V}}_k(t)$ form a basis set in the null space of $\hat{\boldsymbol{H}}_k(t)$. Then, $\boldsymbol{W}_{TX,k}$ is defined as

$$\boldsymbol{W}_{TX,k} = \hat{\boldsymbol{V}}_k^0\boldsymbol{T}_k. \tag{4.4}$$

Here, $\boldsymbol{T}_k$ denotes a nonzero arbitrary matrix which will be used to distribute the transmit data resource adaptively for each user.

Substituting (4.2) and (4.4) into (4.1), we have

$$\boldsymbol{r}_k(t) = \boldsymbol{H}_k(t)\hat{\boldsymbol{V}}_k^0(t)\boldsymbol{T}_k(t)\boldsymbol{s}_k(t) + \boldsymbol{n}(t) \tag{4.5}$$

The optimum matrix $\boldsymbol{T}_k(t)$ can be determined by the E-SDM techniques as stated in the next subsection.

### 4.1.2 Eigenbeam-Space Division Multiplexing method

Let us introduce the equivalent single-user MIMO channel of the $k$-th user as $\boldsymbol{H}_{eq,k} = \boldsymbol{H}_k\hat{\boldsymbol{V}}_k^0(t)$, and the received signal given by (4.5) is rewritten as

$$\boldsymbol{r}_k(t) = \boldsymbol{H}_{eq,k}(t)\boldsymbol{T}_k(t)\boldsymbol{s}_k(t) + \boldsymbol{n}_k(t) \tag{4.6}$$

In order to suppress IStI, the E-SDM method orthogonalizes each single-user MIMO channel by using eigenbeams. Applying the E-SDM technique, the equivalent transmit weight matrix $\boldsymbol{T}_k(t)$ can be determined as

$$\boldsymbol{T}_k(t) = \boldsymbol{V}_{eq,k}(t)\sqrt{\boldsymbol{P}_k(t)}, \tag{4.7}$$

where $\boldsymbol{P}_k(t)$ is the diagonal transmit power matrix for the $k$-th user, and $\boldsymbol{V}_{eq,k}(t)$ is given by the SVD of $\boldsymbol{H}_{eq,k}(t)$ as follows;

$$\boldsymbol{H}_{eq,k}(t) = \boldsymbol{U}_{eq,k}(t)\boldsymbol{\Sigma}_{eq,k}(t)\boldsymbol{V}_{eq,k}^H \tag{4.8}$$

By substituting (4.7) into (4.4), we have

$$\boldsymbol{W}_{TX,k} = \hat{\boldsymbol{V}}_k^0\boldsymbol{V}_{eq,k}\sqrt{\boldsymbol{P}_k}. \tag{4.9}$$

At the receiver side, to demultiplex the received signals, any receive weights such as the MRC or spatial filtering weight based on the MMSE criterion.

## 4.2 Channel Prediction

As stated in the above, the transmit weights, which are determined with the BD scheme and E-SDM method, suppress IUI and IStI for the channels. In this chapter, we assume that the channel changes during the ACK packets are negligibly small and do not affect the channel estimation. The BS, however, sends downlink packets with delay $\tau$ from the ACK packets. The channels change during the delay in time-varying environments where MSs and/or surrounding scatterers move, and we have

$$\boldsymbol{H}_{eq,k}(t+\tau) = \boldsymbol{H}_{eq,k}(t) + \Delta\boldsymbol{H}_{eq,k}(t,\tau). \tag{4.10}$$

The transmit weight matrices $\boldsymbol{W}_{TX,k}(t)$ are outdated for the downlink multi-user transmission. Then, instead of (4.2), we have

$$\begin{aligned}\boldsymbol{H}_{eq,m}(t+\tau)\boldsymbol{W}_{TX,k}(t) &= \{\boldsymbol{H}_{eq,m}(t) + \Delta\boldsymbol{H}_{eq,m}(t,\tau)\}\boldsymbol{W}_{TX,k}(t) \\ &= \begin{cases} \tilde{\boldsymbol{H}}'_{eq,k}(t,\tau) & (m=k) \\ \Delta\boldsymbol{H}_{eq,m}(t,\tau)\boldsymbol{W}_{TX,k}(t) & (m\neq k)\end{cases}.\end{aligned} \tag{4.11}$$

Here,

$$\tilde{\boldsymbol{H}}'_{eq,k}(t,\tau) = \tilde{\boldsymbol{H}}_{eq,k}(t,\tau)\boldsymbol{W}_{TX,k}(t). \tag{4.12}$$

As seen from the (4.11), the outdated transmit weights cause the IUI, $\Delta\boldsymbol{H}_{eq,m}(t,\tau)\boldsymbol{W}_{TX,k}(t)$ for $m \neq k$. Since $\tilde{\boldsymbol{H}}^H_{eq,k}(t,\tau)\tilde{\boldsymbol{H}}_{eq,k}(t,\tau)$ is a diagonal matrix, maximal ration combining at MSs does not cause IStI. The effective downlink channels are, however, not $\tilde{\boldsymbol{H}}_{eq,k}(t)$ but are $\tilde{\boldsymbol{H}}'_{eq,k}(t,\tau)$ due to the delay $\tau$. Since $\tilde{\boldsymbol{H}}^H_{eq,k}(t,\tau)\tilde{\boldsymbol{H}}'_{eq,k}(t,\tau)$ is not a diagonal matrix, MSs suffer from IStI if we employ the maximal ratio combining. Even when the channel estimation is carried out accurately using the ACK packets, the interference is caused in the time-varying channels and the performance of multi-user transmission is deteriorated. If we can predict future channels when data are transmitted by using past channels, IUI and IStI can be decreased. We will briefly describe channel prediction schemes in the following subsection.

### 4.2.1 Channel Prediction Based on AR Model

We present the channel from the $j$-th transmit antenna of the BS to the $i$-th receive antenna of the $k$-th MS at time $t$ by $h_{ij,k}(t)$. The future channel at downlink packet transmission time, $nT_f + \tau$, predicted by the AR-model-based algorithm is given by

$$\hat{h}^A_{ij,k}(nT_f+\tau) = \sum_{m=1}^{p} a_m h_{ij,k}\left((n+1-m)T_f\right) \tag{4.13}$$

Here, $a_m$ are AR coefficients, and $p$ is called the AR model order. The optimum AR coefficients are determined by using the Yule-Waker equation

$$\boldsymbol{R}\boldsymbol{a} = \boldsymbol{r}'. \tag{4.14}$$

The $\boldsymbol{a}$ is the $p$-dimensional vector in (4.14) defined as

$$\boldsymbol{a} = [a_1,\ a_2,\ \cdots,\ a_p]^T, \tag{4.15}$$

where $[\cdot]^T$ denotes the transpose. The $\boldsymbol{R}$ is the $p \times p$ correlation matrix whose $l_1$-th row and $l_2$-th column elements are given by

$$\begin{aligned} r(l_1 - l_2) &= r^*(l_2 - l_1) \\ &= E\{h^*_{ij,k}((n+1-l_1)T_f)h_{ij,k}((n+1-l_2)T_f)\} \\ &= E\{h^*_{ij,k}((n-(l_1-l_2))T_f)h_{ij,k}(nT_f)\}, \end{aligned} \tag{4.16}$$

where $(\cdot)^*$ denotes the complex conjugate and $E\{\cdot\}$ denotes the ensemble average. Also, the $l$-th element of the $p$-th dimensional correlation vector $\boldsymbol{r}'$ is given by

$$r'(l) = E\{h^*_{ij,k}((n+1-l)T_f)h_{ij,k}(nT_f + \tau)\}. \tag{4.17}$$

We need the autocorrelations of channels to solve (4.17). However, it is not easy to accurately estimate autocorrelations in actual environments. We obtained autocorrelations assuming the Jakes' model, and the autocorrelation function is given by

$$E\{h^*_{ij,k}(t-T)h_{ij,k}(t)\} = \boldsymbol{J}_0(2\pi f_D T), \tag{4.18}$$

where $\boldsymbol{J}_0(\cdot)$ is the Bessel function of the first kind of order zero and $f_D$ is the maximum Doppler frequency. Note that we ignore the constant coefficient in (4.18), which does not affect the AR coefficients. Thus, (4.16) and (4.17) are rewritten as

$$\begin{aligned} r(l_1 - l_2) &= r(l_2 - l_1) \\ &= \boldsymbol{J}_0(2\pi f_D(l_1 - l_2)T_f), \end{aligned} \tag{4.19}$$

$$r'(l) = \boldsymbol{J}_0(2\pi f_D(\tau + (l-1)T_f)). \tag{4.20}$$

Substituting (4.19) and (4.18) into (4.14), we can obtain the AR coefficients and compute future channels.

### 4.2.2 Lagrange Extrapolation

We presented AR-model-based prediction in the previous subsection that assumed the Jakes' model. Even in this case, we need the maximum Doppler frequency $f_D$ to obtain the autocorrelations. However, it is not necessarily easy to accurately estimate values in actual environments.

Lagrange extrapolation, on the other hand, is extremely easy to implement. The method does not need either channel autocorrelations or the maximum Doppler frequency. We evaluated linear, second-order, and third-order extrapolations of the Lagrange extrapolation schemes.

A future channel is linearly extrapolated in linear extrapolation with the last two channels and is given by

$$\hat{h}^L_{ij,k}(nT_f+\tau) = h_{ij,k}(nT_f) + \frac{\tau}{T_f}(h_{ij,k}(nT_f) - h_{ij,k}((n-1)T_f)). \tag{4.21}$$

The values predicted by the quadratic function using the last three channels and the cubic function using the last four channels are similarly respectively given by the following equations, respectively.

$$\begin{aligned}
&\hat{h}^S_{ij,k}(nT_f+\tau) = \\
&h_{ij,k}((n-2)T_f) + \frac{(2T_f+\tau)}{T_f}(h_{ij,k}((n-1)T_f) - h_{ij,k}((n-2)T_f)) \\
&+ \frac{(2T_f+\tau)(T_f+\tau)}{2T_f^2}(h_{ij,k}(nT_f) - 2h_{ij,k}((n-2)T_f) + h_{ij,k}((n-2)T_f))
\end{aligned} \tag{4.22}$$

$$\begin{aligned}
&\hat{h}^T_{ij,k}(nT_f+\tau) = \\
&h_{ij,k}(nT_f) - \frac{(2T_f+\tau)(T_f+\tau)\tau}{6T_f^3} \\
&(h_{ij,k}((n-3)T_f) - 3h_{ij,k}((n-2)T_f) + 3h_{ij,k}((n-1)T_f) - h_{ij,k}(nT_f)) \\
&+ \frac{(T_f+\tau)\tau}{2T_f^2}(h_{ij,k}((n-2)T_f) - 2h_{ij,k}((n-1)T_f) + h_{ij,k}(nT_f)) \\
&- \frac{\tau}{T_f}(h_{ij,k}((n-1)T_f) - h_{ij,k}(nT_f))
\end{aligned} \tag{4.23}$$

We can estimate channels by using past channels alone as can be seen from (4.21) $\sim$ (4.23). As a result, the Lagrange scheme is much easier than AR-based extrapolation with respect to implementation.

## 4.3 Analyses of Performance in Channel Predictions

We examined the prediction effects for multi-user MIMO downlink channels in cases of the correlated and uncorrelated Jakes' model and an actual indoor environment. We conducted simulations of a multi-user MIMO E-SDM system by assuming the parameters listed in Tab. 4.1. We assumed that the data rate for each MS was fixed constantly at 4 bps/Hz (4 bits per symbol duration). Because the TX had four antennas and each RX had two antennas, we had either single-stream (16QAM: quadrature amplitude modulation) or two-stream (2 $\times$ QPSK: quaternary phase shift keying) transmission for each RX. Determining the number of streams, modulation scheme, and TX power was done in such a way that the Chernoff upper bound of the BER for each MS had the lowest value [36]. The total TX power per MS was the same. We assumed frequency flat fading channels. The uplink channels were estimated at the TX using pilot symbols in the ACK packets, and the effective

Table 4.1: Simulation parameters.

| | |
|---|---|
| No. of MSs | 2 |
| No. of antennas | TX:4, RX:2 |
| Data rate for each MS | 4 bits/symbol/user |
| Modulation schemes | QPSK, 16QAM |
| Resource control | Minimum BER criterion based on Chernoff upper bound [36] |
| Data burst length in a downlink packet | 128 symbols |
| Frame duration | $T_f = 10$ ms |
| Center frequency | $f_c = 5.275$ GHz |
| Max. Doppler frequency | $f_D$ = 18.6 Hz |
| Thermal noise | Additive white Gaussian noise |
| RX signal processing | MMSE weight |

downlink channels ($\tilde{\boldsymbol{H}}'_k(t,\tau)$) for E-SDM transmission were estimated at both RXs using pilot symbols in the downlink packets. For each uplink channel, $N_p$ pilot symbols multiplied by the transmit weights in each downlink packet were sent for estimation. Because all the pilot symbols were 1 in the simulations, each channel was obtained by averaging the $N_p$ pilot symbols. The effective SNR for channel estimation is $N_p$ times higher than a single pilot symbol case. All the pilot symbols inserted in the packets were transmitted separately in the time domain, and the uplink channels and the effective downlink channels were estimated without interference even in time-varying environments. We assumed that the pilot symbol power for both the uplink channel estimation and the effective downlink channel estimation was equal to that in the duration of data symbol transmission. Each RX determined the minimum mean-squared error (MMSE) weights using its own effective downlink channels. We will explain the propagation environments in the following subsections.

### 4.3.1 Jakes' Model

Propagation channels often experience Rayleigh fading in mobile communications, and the Jakes' model can emulate Rayleigh fading environments [61–63]. The Jakes' model assumed the TX and RXs were positioned as shown in Fig.4.3. The TX and RXs correspond to the BS and MSs that were previously explained. We assumed that there were 13 scatterers uniformly distributed on a ring surrounding each RX, and the angle spread from the TX to each ring of scatterers was equal to $\pi/3$. The number of scatterers, 13, is sufficient for simulating time-correlated Rayleigh fading channels. Also, we do not need to designate the distance between the TX and RXs. The effect of distance attenuation is included in normalized TX power that will be defined in Sect. 4.3.3. Correlations between channels are related with the angle spread from the TX, and are determined without giving

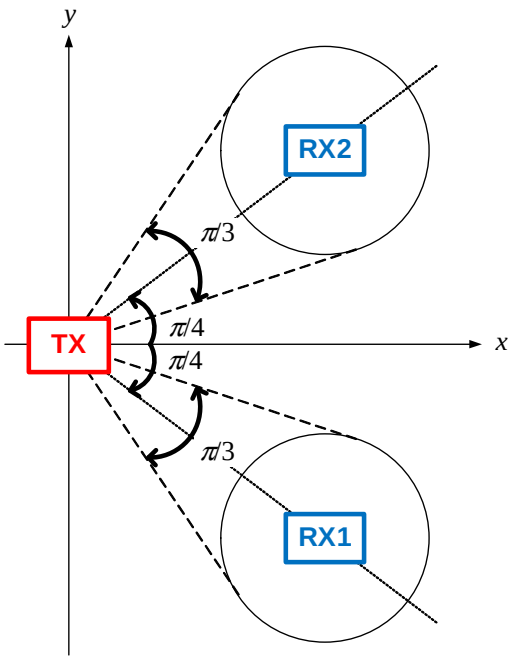


Figure 4.3: Positions of TX and RXs (RX1 and RX2). The TX and RXs correspond to the BS and MSs, respectively.

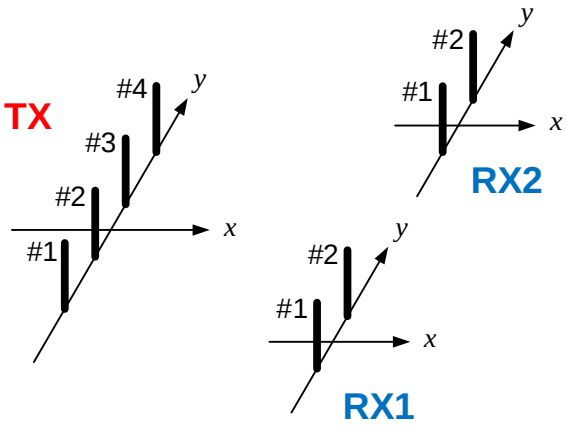


Figure 4.4: Configuration of array.

the distance. Arrays with an omnidirectional antenna spacing of 3 cm (half-wavelength at 5 GHz) were along the $y$-axis, as shown in Fig. 4.4. Here, we evaluated performance for both cases where there were correlations and no correlations between channels.

Since we assumed the Jakes' model, the 13 scatterers distributed incident waves with

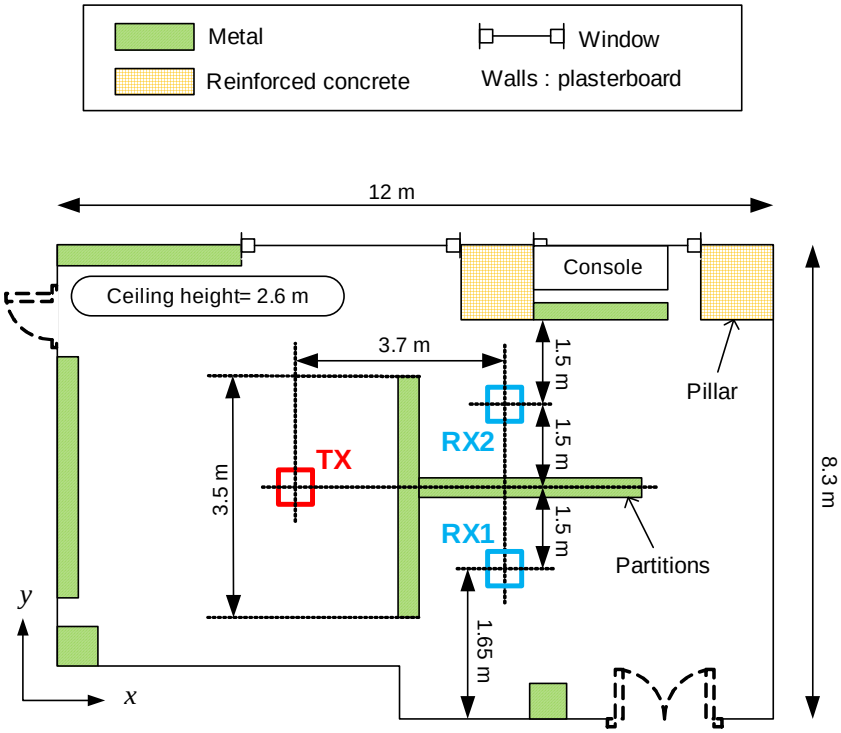


Figure 4.5: Measurement site (top view).

an equal amplitude but with randomly different phases. When the channels had correlations, the phases of the waves rotated by the same amount at the same scatterer. Thus, we could achieve correlated Rayleigh fading environments. However, each scatterer in the uncorrelated case independently and randomly rotated the phase of each incident wave. Then, the channels experienced independent and identically distributed Rayleigh fading. The RXs in both cases moved at a constant velocity, and we obtained time-varying Jakes' environments.

### 4.3.2 Actual Indoor Environment

The campaign to measure the multi-user MIMO system was carried out in a meeting room in a building of the Graduate School of Information Science and Technology at Hokkaido University, as shown in Fig. 4.5. The measurements were the same as those done by Bui et al. [37]. The walls of the room were mostly plasterboard. The room also had reinforced concrete pillars, metal doors, and a metal whiteboard. A four-element TX and two two-element RX linear arrays were placed on three tables in the room. The arrays that consisted of omnidirectional collinear antennas were the same as those in Fig. 4.4. The nominal gain of these antennas on the horizontal plane was about 4 dBi. We examined a non-line-of-sight (NLOS) case where the line-of-sight (LOS) components were blocked by the

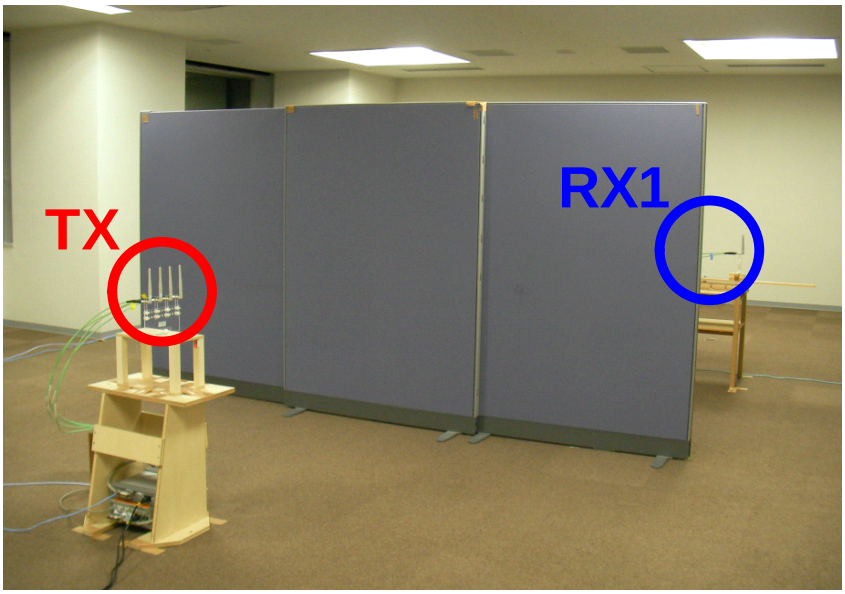


Figure 4.6: Measurement environment.

partitions, as shown in the photograph in Fig. 4.6. Note that RX2 was behind the partitions and it has not been shown in the figure.

The measurement band was from 5.15 to 5.40 GHz (bandwidth = 250MHz), and we obtained 1,601 frequency domain data with 156.25kHz intervals by using a vector network analyzer. Two stepping motors were used on the RX side to move the two RX arrays along the $x$-axis during the experiments. Each step of the motors corresponded to 0.088 mm. The channels were measured at intervals of 0.88 mm, and we had a total of 500 spatial measuring points. As a result, $1,601 \times 500 = 800,500$ MIMO channel response matrices were obtained for each user. Note that the measurement campaign was conducted while there was no one in the room to ensure statistical stationarity of propagation.

### 4.3.3 Analyses of Performance

Figure 4.7 and 4.8 plot the average packet error rates (PERs) with channel predictions for RX1 versus normalized TX power in the Jakes' model for the former and in the indoor environment for the latter. The solid curves with AR(2), AR(3), and AR(4) indicate the PER using AR-model-based predictions of the orders two, three, and four. Similarly, the dotted curves represent performance using Lagrange extrapolation. Linear, Second, and Third in the figures correspond to linear, second-order, and third-order extrapolations. In addition to PER with the predictions, performance without predictions (Non-Prediction) and that of an ideal case are plotted in the figures. When we did not predict channels, we determined the TX weights and other parameters using the CSI obtained from the latest

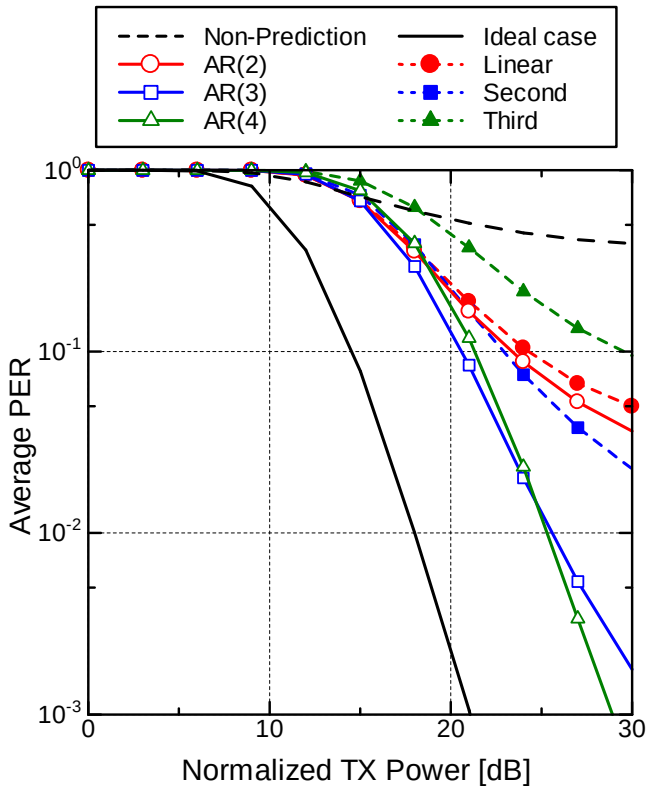


(a) Uncorrelated environment

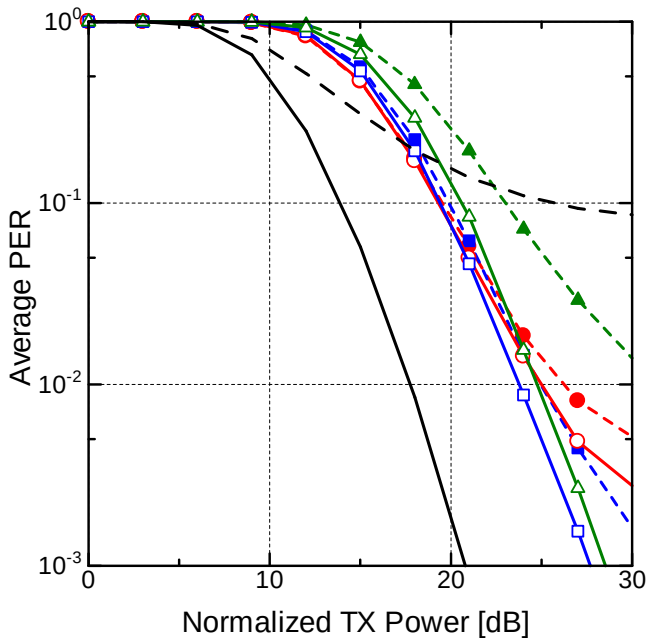


(b) Correlated environment

Figure 4.7: Averaged PER of multi-user MIMO systems for RX1 in case of Jakes' model. $N_p = 1$.

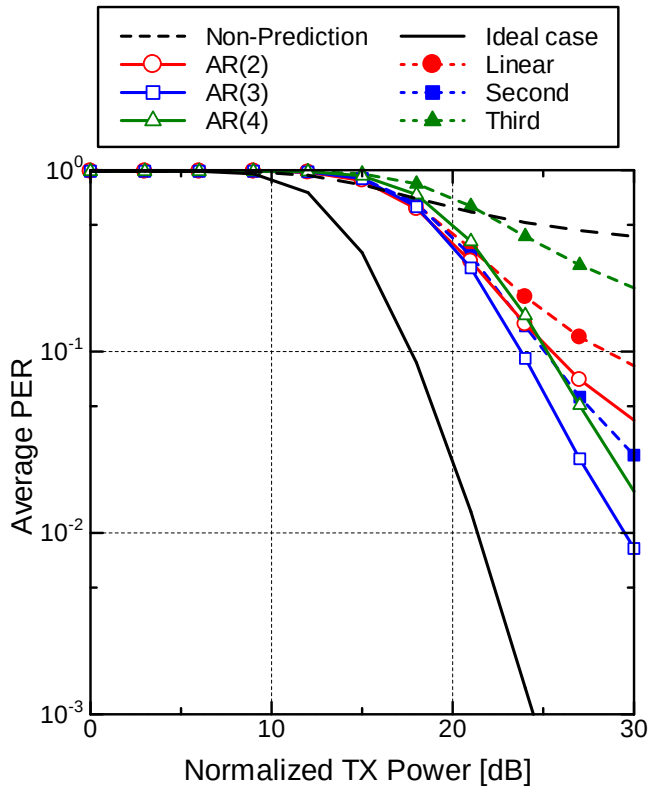


(a) $N_p = 1$

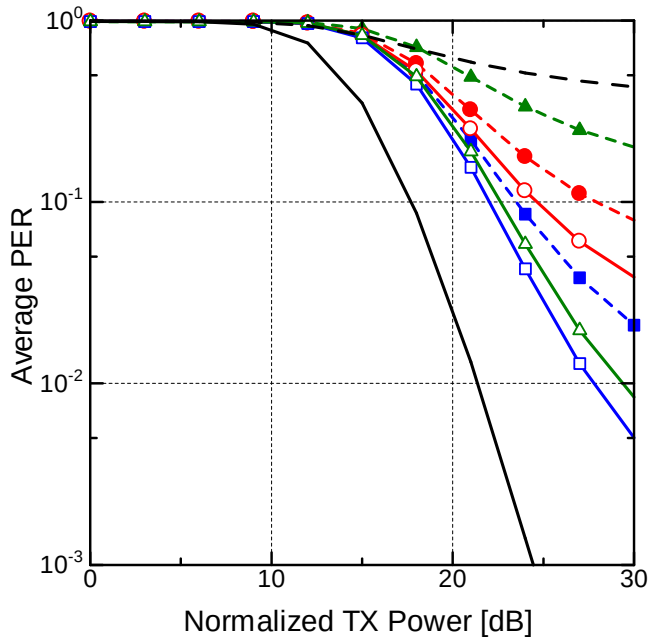


(b) $N_p = 8$

Figure 4.8: Averaged PER of multi-user MIMO systems for RX1 in indoor NLOS environment. RX motion along $x$-axis

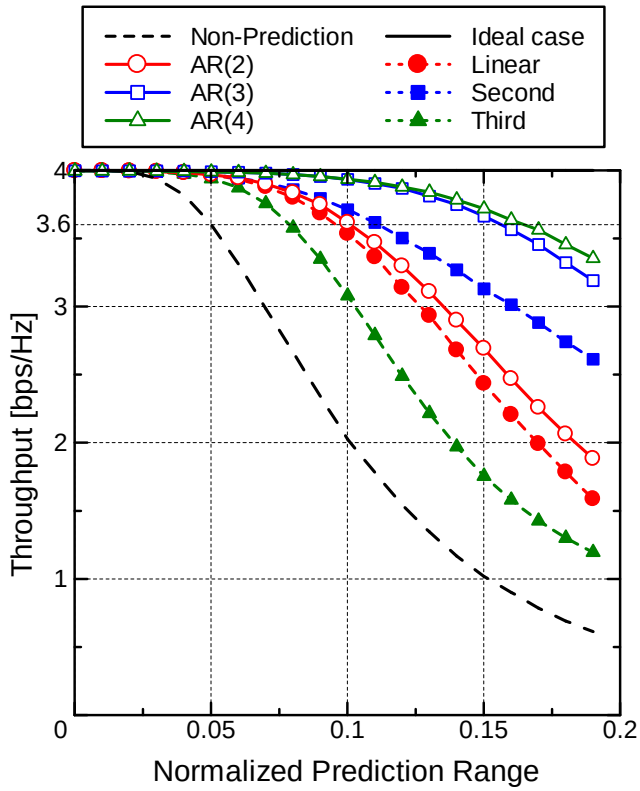


(a) Uncorrelated environment

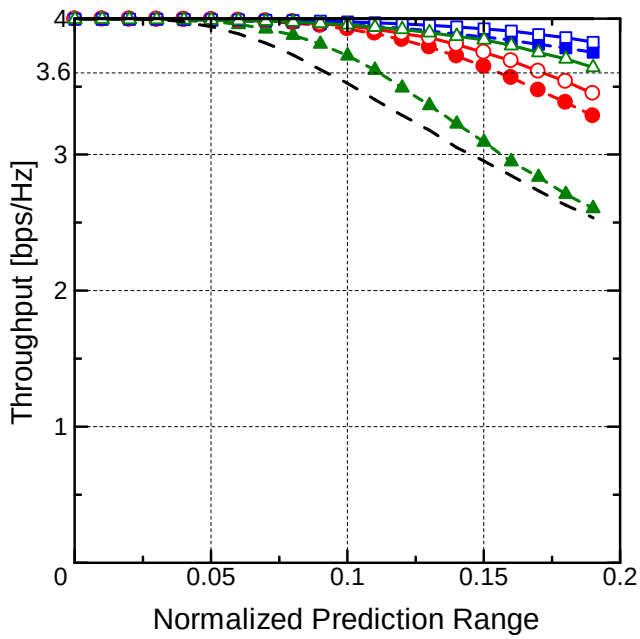


(b) Correlated environment

Figure 4.9: Throughput for RX1 versus normalized prediction range at normalized TX power of 25 dB in case of Jakes' model. $N_p = 1$.

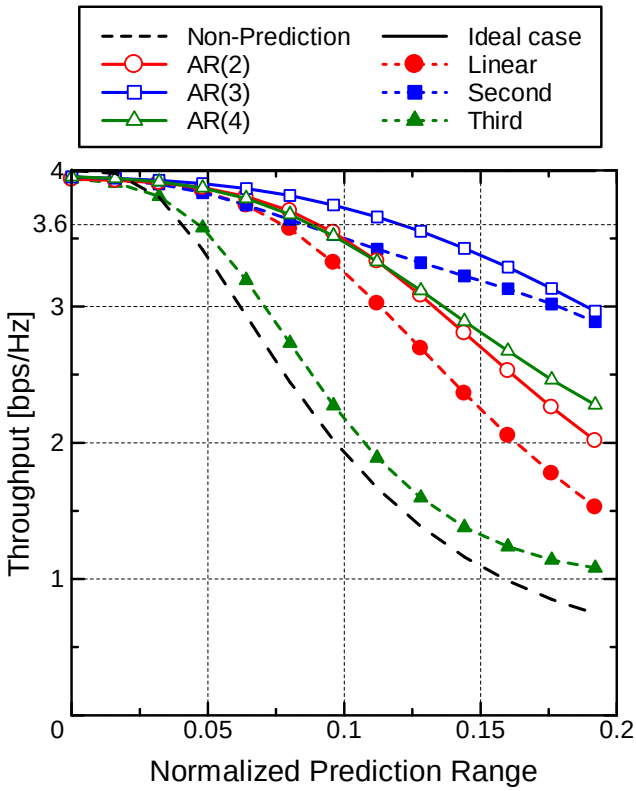


(a) $N_p = 1$

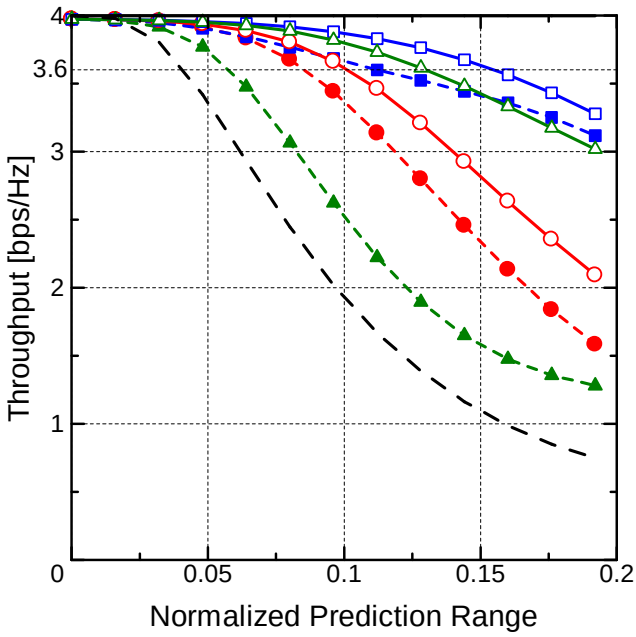


(b) $N_p = 8$

Figure 4.10: Throughput for RX1 versus normalized prediction range at normalized TX power of 25 dB in indoor NLOS environment. RX motion is along $x$-axis.

ACK packet. The ideal case indicated behavior using accurately-predicted channels where not only TX weights but also RX weights were determined based on the correct CSI. The normalized TX power in the Jakes' model is defined as the TX power per MS normalized by the value yielding average $E_s/N_0$ of 0 dB at the single omni-directional antenna receiver when a signal is transmitted from the single omni-directional antenna. Here, $E_s$ denotes the energy received during a symbol interval and $N_0$ denotes the thermal noise power spectrum density. The normalized TX power in the indoor environment is the TX power per MS normalized by the power yielding average $E_s/N_0$ of 0 dB in single-user single-input single-output LOS measurements in an anechoic chamber. Note that $E_s/N_0$ is equal to the signal-to-noise ratio (SNR). We assumed the number of pilot symbols ($N_p$) to estimate channels was one for Figs. 4.7 and 4.8(a), and eight for Fig. 4.8(b). Let us assume that the normalized TX power is $P_{TX,nor}$ in the Jakes' model. Since the pilot symbols in ACK packets are transmitted separately in the time domain, the average SNR for the uplink channel estimation is equal to $P_{TX,nor}$. The average SNR for the effective downlink channel estimation is equal to the mean square of each element in $\tilde{\boldsymbol{H}}'_k(t,\tau)$. It should be noted that the normalized TX power $P_{TX,nor}$ is included in the weights as stated in [37]. The average SNR for the channel estimation in the indoor environment can be similarly evaluated. In addition, we assumed that the maximum Doppler frequency was 18.6 Hz at the center frequency $f_c = 5.275$ GHz, and the transmission delay $\tau$ of the downlink packet from the ACK packet was 5 ms.

We can see high error floor in Figs. 4.7 and 4.8 when we did not predict the channels. The TX side transmitted at most two streams to each MS. Each MS with two antennas could reduce the IStI because the RX weights were determined based on the MMSE criterion. The RX sides could not, however, reduce the IUI. The TX weights were not optimum because of channel transition during the delay of 5 ms, and they could not suppress the IUI. The error floor for the Jakes' model in the uncorrelated environment (Fig. 4.7(a)) was higher than that in the correlated environment (Fig. 4.7(b)) since the channels independently varied in the uncorrelated environment. In contrast, every channel prediction scheme improved performance in higher TX power regions. It can be seen from Figs. 4.7 and 4.8 that AR-model-based prediction with the order $p$ of three provides slightly better PER than that with the $p$ of four except where the normalized TX power is higher than 25 dB in the uncorrelated Jakes' environment (Fig. 4.7(a)). If the estimated channels used for predictions are accurate in the Jakes' model cases, the higher the order is, the better the PER that AR-model-based prediction provides. This is because the autocorrelations were obtained assuming the Jakes' model as given by Eqs.(4.19) and (4.20). The estimated channels, however, contained errors since they were obtained with finite pilot symbols. Hence, AR-model-based prediction with a higher order did not necessarily provide better PER even in the Jakes' model cases. It is interesting that predictions assuming the Jakes' model could also achieve significant reductions in PER in the indoor environments (Fig. 4.8).

Second-order extrapolation achieved the best PER for the Lagrange extrapolation schemes, which is almost the same as that obtained from AR-model-based prediction with the order of four except for the uncorrelated Jakes' model. Third-order extrapolation, on the other

hand, had the worst prediction. When we used Lagrange extrapolation, the predicted channels were obtained by calculating a function that had every data point used fro prediction. Thus, when the order was higher, the function vibrated greatly and degraded the accuracy of prediction.

It can be seen from Fig. 4.8 that the PER for $N_p = 8$ was better than that for $N_p = 1$. When there were more pilot symbols, channels were estimated more accurately, and this improved performance.

Figures 4.9 and 4.10 plot the throughput for RX1 versus the normalized prediction range. The normalized prediction range is a distance $(l)$ where the MSs move during the delay time $(\tau)$ normalized by the wavelength $(\lambda)$ at the center frequency $(f_c)$. The value is written using the maximum Doppler frequency $(f_D)$ as

$$\frac{l}{\lambda} = \frac{v\tau}{\lambda} = \left(\frac{v}{c} f_c\right) \tau = f_D \tau, \tag{4.24}$$

where $v$ is the velocity of the MSs. The figures plot throughput when we predicted channels at positions with distances of the range from RX1. We changed the normalized prediction range from 0 to 0.186 in the simulations by varying $\tau$ from 0 to 10 ms for the fixed value of $f_D = 18.6$ Hz. Throughput is given by 4 $\times$ (1 - Average PER) bps/Hz because the data rate for each MS is 4 bps/Hz. We assumed that the normalized TX power was 25 dB. Note that the throughput for the ideal case is 4 bps/Hz independently of the normalized prediction range.

As can be seen from these figures, if we did not use the prediction schemes, throughput degraded seriously when the normalized prediction range increased. We considered a normalized prediction range where throughput was maintained above 3.6 bps/Hz to be a 10 $\%$ degradation value from the ideal case. The normalized prediction range for the uncorrelated Jakes' model (Fig. 4.9(a)) was wider than 0.15 for the AR-model-based scheme with $p$ of three or four, and was wider than 0.1 for second-order extrapolation. Throughput was higher than 3.6 bps/Hz over the whole range using the three prediction schemes for the correlated Jakes' model (Fig. 4.9(b)). It should be noted that this performance was obtained using one pilot symbol for each channel ($N_p = 1$). However, throughput in the indoor environment for $N_p = 1$ (Fig. 4.10(a)) was worse than that in the Jakes' model cases. Performance could, however, be improved by using more pilot symbols. It can be seen from Fig. 4.10(b) that the throughput for $N_p = 8$ is above 3.6 bps/Hz in normalized prediction ranges wider than 0.1 if we use second-order extrapolation or AR-model-based prediction with $p$ of three or four.

## 4.4 Conclusions

In this chapter, the author investigated what effects channel predictions using an AR-model-based scheme and Lagrange extrapolation would have on a multi-user MIMO system. These considerations were done in the presence of channel estimation error. The

author found that every prediction scheme could improve performance. The effect of prediction differed depending on the order of the AR model in the AR-mode-based predictor. Lagrange extrapolation could provide performance comparable to that of AR-model-based prediction without statistical quantities that were not necessarily easy to estimate. Furthermore, the author showed that second-order extrapolation could predict channels in normalized prediction ranges over within a throughput degradation of $10\%$. Since Lagrange extrapolation is easy to implement, prediction schemes using it can play important roles in multi-user MIMO systems.

# Chapter 5

# Conclusions and Future Work

## 5.1 Summary

In this dissertation, in order to realize the future IoT systems, the author has examined advanced systems for long-range wireless network in terms of "high reliability transmission", "high data rate transmission", and "multi-user transmission".

First, Chapter 1 explained about the background and motivation of the dissertation based on the usage scenarios and requirements in the future IoT system which is defined by ITU-R. Chapter 2 proposed the pilot-less narrow-band coherent FSK system applying phase rotated transmit diversity as an advanced system with high reliability. The phase rotated transmit diversity reduces the phase discontinuity between the space-time coded FSK symbols, and therefore suppresses any envelope fluctuations. The proposed pilot-less coherent FSK schemes estimates the channel parameters by using the feature that the initial phase of an FSK symbols is uniquely determined, instead of inserting known pilot symbols. By using computer simulation, the author verified that the proposed diversity techniques suppresses the envelope fluctuation and yields a performance improvement of about 10 dB at CDF=$10^{-2}$. Furthermore, the proposed coherent system showed improved performance without inserting known pilot symbols even in the event of high-speed movement.

In Chapter 3, the author investigated the high data rate transmission scheme. To increase the communication capacity, the author examined the two-dimensional diversity approach which exploits frequency and spatial diversity simultaneously by serially concatenating spectral precoding and PN-DSTBC. However, a naive concatenation decreases the spectral decoder performance due to the imbalance of equivalent noise variances over transmit frequencies at PN-DSTBC decoder. Hence, the author proposed the modified approach which compensates the equivalent noise imbalance by applying equalized PN-DSTBC decoder in order to address the issues. The computer simulation results showed that the modified approach yields the performance improvement at any modulation schemes and at

any number of transmit frequencies. Furthermore, the performance gain of the proposed approach is about 4dB at uncoded BER=$10^{-4}$ in the case of 64QAM and two transmit frequencies.

Chapter 4 examined multi-user MIMO systems. Although BD scheme and E-SDM scheme suppresses interferences by applying beamforming weights based on channel responses, channels change during the time intervals between the time to determine parameters and the transmission time degrades the performance in time-varying environments. Therefore, the author applied the channel prediction techniques, AR-mode-based scheme and Lagrange extrapolation, to resolve the issue in multi-user MIMO system. In cases of the Jakes' model and an actual indoor environment, the performance evaluation showed that each scheme yields the performance improvement and suppresses the throughput degradation under 10 $\%$ in normalized prediction ranges over 0.1.

## 5.2 Future Work

Although the author has investigated the advanced systems for the future IoT, there are several issues left that should be considered for future work.

- Multipath environment
  In Chapter 2 and 3, since the author assumed the narrowband system, the performance evaluations were conducted in flat fading environments. However, considering severe environments, it would be important to confirm a multipath tolerance of the proposed schemes. Moreover, the author should be examine the countermeasures for multipath environments.

- Implementation
  Except for some parts of Chapter 4, the author investigated the performance improvement of the proposed system by using computer simulations through all th work in the dissertation. The author thinks that it is necessary to investigate implementability of the proposed system not only by computer simulations but also by using actual processing devices.

# References


[1] Cisco, "Cisco Visual Networking Index: Global Mobile Data Traffic Forecast Update, 2017–2022, " Cisco White Paper, Feb. 2019.

[2] K. Ashton, "That 'Internet of Things' Thing," *RFID Journal*, Jun. 2019.

[3] ITU, "The Internet of Things," ITU Internet Reports, Nov. 2005.

[4] 5G Americas, "5G-The Future of IoT," 5G Americas White Paper, July 2019.

[5] G. A. Akpakwu, B. J. Silva, G. P. Hancke, and A. m. Abu-Mahfouz, "A Survey on 5G Networks for the Internet of Things: Communication Technologies and Challenges," *IEEE Access*, vol.6, pp.3619–3647, 2018.

[6] D. Evans, "The Internet of Things, How the Next Evolution of the Internet Is Changing Everything," Cisco White Paper, pp.1–11, 2011.

[7] S. Andreev, O. Galinina, A. Pyattaev, M. Gerasimenko, T. Tirronen, J. Torsner, J. Sachs, M. Dohler, and Y. Koucheryavy, "Understanding the IoT Connectivity Landscape: A Contemporary M2M Radio Technology Roadmap," *IEEE Commun. Mag.*, vol.53, no.9, pp.32–40, Sept. 2015.

[8] ITU, "Disruptive technologies and their use in disaster risk reduction and management," *ITU GET-19*, March 2019.

[9] J. J. Wellington, and P. Ramesh, "Role of Internet of Things in disaster management," *Proc. 2017 ICIIECS*, pp.1–4, March 2017.

[10] GSMA White Paper, "3GPP Low Power Wide Area Technologies," Oct. 2016.

[11] S. Mumtaz, A. Alsohaily, Z. Pang, A. Rayles, K. F. Tsang, and J. Rodriguez, "Massive Internet of Things for Industrial Applications," *IEEE Ind. Electron. Mag.*, vol.11, no.1, pp.28–33, March 2018.

[12] U. Raza, P. Kulkarni, and M. Sooriyabandara, "Low Power Wide Area Networks: An Overview," *IEEE Commun. Surv, & Tut.*, vol.19, no.2, pp.855–873, Secondquarter 2017.

[13] K. Mekki, E. Bajic, F. Chaxel, and F. Meyer, "A comparative study of LPWAN technologies for large-scale IoT," *ICT Express*, vol.5, issue 1, pp.1–7, 2019.

[14] LoRa Alliance, "LoRaWAN™1.1 Specification," Oct. 2017.

[15] Sigfox, "Sigfox Technical Overview," May 2017.

[16] 3GPP TS36.304 V13.2.0, "User Equipment (UE) procedures in idle mode," June 2016.

[17] 3GPP TR36.888 V12.0.0, "Study on provision of low-cost Machine Type Communications (MTC) User Equipments (UEs) based on LTE,," June 2013.

[18] V. Saxena, A. Wallén, T. Tirronen, H. S. Razaghi, J. Bergman, and Y. Blankenship, "On the achievable Coverage and Uplink Capacity of Machine-Type Communications (MTC) in LTE Release 13," *Proc. IEEE VTC-Fall 2016*, pp.1–6, Sept. 2016.

[19] 3GPP TS22.368 V15.0.0, "Service requirements for Machine-Type Communications (MTC)," July 2019.

[20] 3GPP TS32.410 V9.0.0, "Key Performance Indicators (KPI) for UMTS and GSM," Sept. 2009.

[21] ETSI TS102.689, V1.1.1, "Machine-to-Machine communications (M2M); M2M service requirements," Oct. 2010.

[22] ETSI TS122.368 V13.1.0, "Service requirements for Machine-Type Communications (MTC)," March 2016.

[23] ITU-R, "IMT Vision - Framework and overall objectives of the future development of IMT for 2020 and beyond," Recommendation ITU-R M.2083-0, Sept. 2015.

[24] S. M. Alamouti, "A Simple Transmit Diversity Technique for Wireless Communications," *IEEE J. Sel. Areas Commun.*, vol.16, no.8, pp.1451–1458, Oct. 1998.

[25] P. Ho, S. Zhang, and P. Y. Kam, "Space-Time FSK: An Implicit Pilot Symbol Assisted Modulation Scheme," *IEEE Trans. on Commun.*, vol.6, no.7, pp.2602–2611, July 2007.

[26] R. W. Schafer, and L. R. Rabiner, "A Digital Signal Processing Approach to Interpolation," *Proc. IEEE*, vol.61, pp.692–702, June 1973.

[27] E. Semaan, F. Harrysson, A. Furuskär, and H. Asplund, "Outdoor-to-Indoor Coverage in High Frequency Bands," *2014 IEEE Globecom Workshop*, pp.393–398, Dec. 2014.

[28] S. R. Lamas, D. González G, and J. Hämäläinen, "Indoor Planning Optimization of Ultra-dense Cellular Networks at High Carrier Frequencies," *Proc. IEEE WCNCW 2015*, pp.23–28, March 2015.

[29] F. Riera-Palou and G. Femenias, "Exploiting Frequency Diversity in SDM/STBC Multicarrier Systems," *2009 Radio and Wireless Symposium*, pp.324–327, Jan. 2009.

[30] E. B. Fluckiger, F. Oggier, and E. Viterbo, "New Algebraic Constructions of Rotated $Z^n$-Lattice Constellations for the Rayleigh Fading Channel," *IEEE Trans. Inform. Theory*, vol.50, no.4, pp.702–714, April 2004.

[31] V. Tarokh and H. J. Jafarkhani, "A Differential Detection Scheme for Transmit Diversity," *IEEE J. Select. Areas Commun.*, vol.18, no.7, pp.1169-1174, July 2000.

[32] C. S. Hwang, S. H. Nam, J. Chung, and V. Tarokh, "Differential Space Time Block Codes Using Nonconstant Modules Constellations," *IEEE Trans. Signal Process.*, vol.51, no.11, pp.2955–2964, Nov. 2003.

[33] S. Umeda, A. Okazaki, H. Nishimoto, K. Tsukamoto, K. Yamaguchi, and A. Okamura, "Cell Structure for High-speed Land-mobile Communications," *IEEE VTC2015-Fall*, pp.1–5, Sept. 2015.

[34] Q. H. Spencer, A. L. Swindlehurst, and M. Haadt, "Zero-forcing methods for downlink spatial multiplexing in multiuser MIMO channels," *IEEE Trans. Signal Processing*, vol, 52, no. 2, pp.461–471, Feb. 2004.

[35] R. L. U. Choi and R. D. Murch, "A transmit preprocessing technique for multiuser MIMO systems using a decomposition approach," *IEEE Trans. Wireless Commun.*, vol. 3, Issue. 1, pp. 20–24, Jan. 2004.

[36] K. Miyashita, T. Nishimura, T. Ohgane, Y. Ogawa, Y. Takatori, and K. Cho, "High data-rate transmission with eigenbeam-space division multiplexing (E-SDM) in a MIMO channel," *Proc. IEEE VTC 2002 Fall*, vol. 3, pp. 1302–1306, Sept. 2002.

[37] H. P. Bui, Y. Ogawa, T. Nishimura, and T. Ohgane, "Performance evaluation of a multi-user MIMO system with prediction of time-varying indoor channels," *IEEE Trans. Antennas and Propagat.*, vol. 61, no. 1, pp. 371–379, Jan. 2013.

[38] A. Duel-Hallen, "Fading channel prediction for mobile radio adaptive transmission systems," *Proc. IEEE*, vol. 95, no. 12, pp. 2299–2313, Dec. 2007.

[39] J. B. Andersen, J. Jensen, S. H. Jensen, and F. Frederiksen, "Prediction of future fading based on past measurements," *IEEE VTC 1999 Fall*, vol. 1, pp. 151–155, Sept. 1999.

[40] T. Eyceoz, A. Duel-Hallen, and H. Hallen, "Deterministic channel modeling and long range prediction of fast fading mobile radio channels," *IEEE Communications Letters*, vol. 2, pp. 254–256, Sept. 1998.

[41] N. Palleit and T. Weber, "Channel prediction in multiple antenna systems," *Smart Antennas (WSA), 2012 International ITG Workshop on*, pp. 1–7, March 2012.

[42] T. Ekman, "Prediction of mobile radio channel - Modeling and design," Ph. D. dissertation, Uppsala University, Uppsala, Sweden, 2002.

[43] L. Dong, G. Xu, and H. Ling, "Prediction of fast fading mobile radio channels in wideband communication systems," *Proc. IEEE GLOBECOM*, vol. 6, pp.3287–3291, Nov. 2001.

[44] K. E. Baddour and N. C. Beaulieu, "Autoregressive modeling for fading channel simulation," *IEEE Trans. Wireless Commun.*, vol. 4, pp. 1650–1662, July 2005.

[45] K. Yamaguchi, H. P. Bui, Y. Ogawa, T. Nishimura, and T. Ohgane, "Considerations on a multi-user MIMO system using channel prediction based on an AR model," *Proc. IEEE AP-S/URSI 2013*, July 2013.

[46] Y. Ogawa, K. Yamaguchi, H. P. Bui, T. Nishimura, and T. Ohgane, "Behavior of a multi-user MIMO system in time-varying environments," *IEICE Trans. Commun.*, vol. E96–B, no. 10, pp. 2364–2371, Oct. 2013.

[47] R. W. Schafer and L. Rabiner, "A digital signal processing approach to interpolation," *Proc. IEEE*, vol. 61, pp. 692–702, June 1973.

[48] H. Matsui and A. Hirose, "Nonlinear prediction of frequency-domain channel parameters for channel prediction in fading and fast Doppler-shift change environment," *Proc. ISAP2012*, Oct./Nov. 2012.

[49] K. Yamaguchi, M. Higashinaka, H. Sano, A. Okamura, T. Ohgane, and T. Nishimura, "A Pilot-less Narrowband Coherent FSK System Applying Phase Rotated Transmit Diversity with Suppression of Envelope Fluctuation," *IEICE Trans. Commun. (Japanese Edition)*, vol.J102-B, no.2, pp.1–10, Feb. 2020.

[50] K. Yamaguchi, N. Gresset, H. Nishimoto, A. Okazaki, H. Sano, S. Umeda, K. Tsukamoto, and A. Okamura, "An Equalization of PN-DSTBC for Concatenating with Spectral Precoding," *IEICE Trans. Fundamentals*, vol.E102-A, no.3, pp.544–552, Mar. 2019.

[51] K. Yamaguchi, H. P. Bui, Y. Ogawa, T. Nishimura, and T. Ohgane, "Channel Prediction Techniques for a Multi-User MIMO System in Time-Varying Environments," *IEICE Trans. Commumn.*, vol.E97-B, no.12, pp.2747–2755, Dec. 2014.

[52] K. Ozaki, M. Higashinaka, A. Okazaki, and F. Ishizu, "A Study on PAPR Reduction Technique in MFSK/DS Block Transmission," *IEICE Trans. Commun. (Japanese Edition)*, vol.J98-B, no.1, pp.53–64, Jan. 2015.

[53] M. Faulkner, "The Effect of Filtering on the Performance of OFDM Systems," *IEEE Trans. Veh. Technol.*, vol.49, no.5, pp.1877–1884, 2000.

[54] Y. Liu, "Bit-Interleaving in Fast FH/SSMA Systems with $M$-FSK Modulation," *IEEE Trans. on Commun.*, vol.6, no.9, pp.3154–3159, Sept. 2007.

[55] T. S. Rappaport, *Wireless Communications: Principles and Practice*, Prentice Halls, Second edition, Jan. 2002.

[56] K. Kim, J. Park, Y. Kim, and J. Kim, "Low-Complexity Soft-ML Detection Algorithm for Modified-DCM in WiMedia UWB Systems," *IEICE Trans. Commun.*, vol.E96-B, no.3, pp.910–913, March 2013.

[57] H. Matsuoka, S. Sampei, N. Morinaga, and Y. Kamio, "Adaptive Modulation System with Punctured Convolutional Code for High Quality Personal Communication Systems," *IEICE Trans. Commun.*, vol.E79-B, no.3, pp.328–334, March 1996.

[58] 3GPP TR 38.900 (V15.0.0), "Study on channel model for frequency spectrum above 6 GHz (Release 15)," June 2018.

[59] M. K. Samimi, G. R. MacCartney, S. Sun, and T. S. Rappaport, "28 GHz Millimeter-Wave Ultrawideband Small-Scale Fading Models in Wireless Channels," *IEEE VTC2016-Spring*, May 2016.

[60] S. Sun, H. Yan, G. R. MacCartney, and T. S. Rappaport, "Millimeter Wave Small-Scale Spatial Statistics in an Urban Microcell Scenario," *2017 IEEE ICC*, pp.1–7, May 2017.

[61] W. C. Jakes, *Microwave Mobile Communications*, pp.13–17, Wiley IEEE Press, Piscataway, NJ, 1994.

[62] P. Dent, G. E. Bottomley, and T. Croft, "Jakes fading model revisited," *Electro. Lett.*, vol.29, no.13, pp.1162–1163, June 1993.

[63] H. Iwai, *Radio Propagation in Mobile Communications*, Fundamental Knowledge for Simulation Analysis of Wireless Communication, pp.88–94, Corona Publishing, Tokyo, 2012. (in Japanese)

# Acknowledgement

I would like to express my sincere appreciation to Professor Takeo Ohgane, Faculty of Information Science and Technology, Hokkaido University, for constructive discussions and generous support.

I am also grateful to Professor Yoshikazu Miyanaga, Professor Kunimasa Saitoh, and Associate Professor Toshihiko Nishimura, Faculty of Information Science and Technology, Hokkaido University, for helpful suggestions and observations.

I wish express the deepest appreciation to Emeritus Professor Yasutaka Ogawa, Faculty of Information Science and Technology, Hokkaido University, for the continuing guidance end encouragement.

I am indebted to Dr. T. Nakakawaji, Dr. K. Kusunoki, Dr. H. Miyashita, Dr. A. Okamura, and Mr. H. Aruga of Mitsubishi Electric Corporation for their supports and encouragement.

I owe my deepest gratitude to Mr. A. Okazaki, Dr. H. Sano, Dr. M. Higashinaka, Dr. H. Nishimoto of Mitsubishi Electric Corporation, and Dr. N. Gresset of Mitsubishi Electric R&D Centre Europe for their valuable advice and cooperation.

I wish to thank the members in Wireless Transmission Group and other groups, Communication Technology Department, Information Technology R&D Center, Mitsubishi Electric Corporation, for helpful suggestions and observations.

With insightful comments and supports from all of them, I could enrich my view of research along with creating the work in the dissertation.

Last, I would like to thank my family and friends for their unconditional love and support.

*Kanako Yamaguchi*

*March 2020*

# List of Publications and Awards

## Journals

[1] Kanako Yamaguchi, Huu Phu Bui, Yasutaka Ogawa, Toshihiko Nishimura, and Takeo Ohgane, "Channel Prediction Techniques for a Multi-User MIMO System in Time-Varying Environments," IEICE Trans. Commun., vol.E97-B, no.12, pp.2747–2755, Dec. 2014.

[2] Kanako Yamaguchi, Nicolas Gresset, Hiroshi Nishimoto, Akihiro Okazaki, Hiroyasu Sano, Shusaku Umeda, Kaoru Tsukamoto, and Atsushi Okamura, "An Equalization of PN-DSTBC for Concatenating with Spectral Precoding," IEICE Trans. Fundamentals, vol.E102-A, no.3, pp.544–552, Mar. 2019.

[3] Kanako Yamaguchi, Masatsugu Higashinaka Hiroyasu Sano, Atsushi Okamura, Takeo Ohgane, and Toshihiko Nishimura, "A Pilot-less Narrowband Coherent FSK System Applying Phase Rotated Transmit Diversity with Suppression of Envelope Fluctuation," IEICE Trans. Commun. (Japanese Edition), vol.J102-B, no.2, pp.100–109, Feb. 2020.

## International Conference

[1] Kanako Yamaguchi, Yasutaka Ogawa, Toshihiko Nishimura, and Takeo Ohgane, "Formulation of a Frequency Correlation for a Multiple-Antenna System," 2011 International Symposium on Antennas and Propagation (ISAP2011), WeE2-1, Jeju, Korea, Oct. 2011.

[2] Kanako Yamaguchi, Yasutaka Ogawa, Toshihiko Nishimura, and Takeo Ohgane, "Considerations on a Frequency Correlation for Distributed Antenna System," 2012 International Symposium on Antennas and Propagation (ISAP2012), POS2-25, Nagoya, Japan, Oct./Nov. 2012.

[3] Kanako Yamaguchi, Huu Phu Bui, Yasutaka Ogawa, Toshihiko Nishimura, and Takeo Ohgane, "Considerations on a Multi-User MIMO System Using Channel Prediction Based on an AR Model," 2013 IEEE Antennas and Propagation Society International Symposium (IEEE AP-S 2013), pp.550–551, Orlando, USA, July 2013.

[4] Hiroshi Nishimoto, Akihiro Okazaki, Yusuke Kinoshita, Kaoru Tsukamoto, Shusaku Umeda, Kazuyoshi Tsuji, Kanako Yamaguchi, and Atsushi Okamura, "Millimeter-wave Train Radio Communication System Based on Linear Cell Concept," The International Symposium on Speed-up and Sustainable Technology for Railway and Maglev Systems (STECH 2015), pp.1–12, Chiba, Japan, Nov. 2015.

[5] Shusaku Umeda, Akihiro Okazaki, Hiroshi Nishimoto, Kaoru Tsukamoto, Kanako Yamaguchi, and Atsushi Okamura, "Cell Structure for High-speed Land-mobile Communications," 2015 IEEE Vehicular Technology Coneference (VTC2015-Fall), pp.1–5, Boston, USA, Sept. 2015.

[6] Kanako Yamaguchi, Nicolas Gresset, Hiroshi Nishimoto, Akihiro Okazaki, Shusaku Umeda, Kaoru Tsukamoto, Hiroyasu Sano, and Atsushi Okamura, "Two-dimensional Diversity with Serial Concatenation of Spectral Precoding and DSTBC," The International Symposium on Information Theory and Its Applications (ISITA 2016), pp.375–379, Monterey, USA, Oct. 2016.

[7] Kanako Yamaguchi, Masatsugu Higashinaka, Hiroyasu Sano, Atsushi Okamura, Takeo Ohgane, and Toshihiko Nishimura, "A Narrow-Band Coherent FSK Transmission System Using Phase Rotated Transmit Diversity with Suppression of Envelope Fluctuation," 2019 IEEE Vehicular Technology Conference (VTC2019-Fall), Honolulu, USA, Sept. 2019.

## Domestic Conference

[1] Kanako Yamaguchi, Huu Phu Bui, Yasutaka Ogawa, Toshihiko Nishimura, and Takeo Ohgane, "Considerations on a Multi-User MIMO System Using Channel Prediction Based on an AR Model in Time-Varying Environments," Proceedings of the 2013 IEICE General Conference, B-1-27, p.217, Gifu, Japan, March 2013 (in Japanese).

[2] Kanako Yamaguchi, Yasutaka Ogawa, Toshihiko Nishimura, and Takeo Ohgane, "Considerations on Prediction Effects of Multi-User MIMO Channels in Time-Varying Environments," Technical Report of IEICE Antennas and Propagation, AP2013-107, pp.43–48, Matsue, Japan, Nov. 2013 (in Japanese).

[3] Kanako Yamaguchi, Yasutaka Ogawa, Toshihiko Nishimura, and Takeo Ohgane, "Considerations on a Multi-User MIMO System Using Channel Prediction in the Presence of Channel Estimation Error," Proceedings of the 2014 IEICE General Conference, B-1-216, p.216, Niigata, Japan, March 2014 (in Japanese).

[4] Hiroshi Nishimoto, Akinori Nakajima, Takehiko Nishide, Kaoru Tsukamoto, Shusaku Umeda, Kanako Yamaguchi, Akihiro Okazaki, and Atsushi Okamura, "Performance Improvement of Time-domain Encoded SFBC for Single-carrier Block Transmission over Fast-fading Multipath Channels," Technical Report of IEICE Radio Communication Systems, RCS2014-189, pp.183–188, Tokyo, Japan, Oct. 2014 (in Japanese).

[5] Kanako Yamaguchi, Nicolas Gresset, Hiroshi Nishimoto, Shusaku Umeda, Kaoru Tsukamoto, Akihiro Okazaki, and Atsushi Okamura, "Serial Concatenation Approach of Spectral Precoding and DSTBC Enabling Two-dimensional Diversity," Technical Report of IEICE Radio Communication Systems, RCS2015-49, pp.19–24, Sapporo, Japan, June 2015 (in Japanese).

[6] Kanako Yamaguchi, Nicolas Gresset, Hiroshi Nishimoto, Shusaku Umeda, Kaoru Tsukamoto, Akihiro Okazaki, and Atsushi Okamura, "Performance Improvement of Frequency-Space Two-dimensional Diversity by Optimizing DSTBC Decoder Output," Proceedings of the 2015 IEICE Society Conference, B-5-23, p.285, Sendai, Japan, Sept. 2015 (in Japanese).

[7] Kanako Yamaguchi, Nicolas Gresset, Hiroshi Nishimoto, Shusaku Umeda, Kaoru Tsukamoto, Akihiro Okazaki, and Atsushi Okamura, "Performance Evaluation of Frequency-Space Two-dimensional Diversity by Applying Forward Error Correction," Proceedings of the 2016 IEICE General Conference, B-5-96, p.489, Fukuoka, Japan, March 2016 (in Japanese).

[8] Kanako Yamaguchi, Nicolas Gresset, Hiroshi Nishimoto, Shusaku Umeda, Kaoru Tsukamoto, Akihiro Okazaki, and Atsushi Okamura, "Reduction in Symbol Replica Cnadidates for MLD Decoding over Spectrally-precoded Diversity Transmission," Proceedings of the 2016 IEICE Society Conference, B-5-20, p.290, Sapporo, Japan, Sept. 2016 (in Japanese).

[9] Kanako Yamaguchi, Kaoru Tsukamoto, Hiroyasu Sano, and Atsushi Okamura, "Optimization of Precoding Matrix for Frequency-Space Two-dimensional Diversity Method," Proceedings of the 2017 IEICE General Conference, B-5-8, p.344, Nagoya, Japan, March 2017 (in Japanese).

[10] Kanako Yamaguchi, Hiroshi Nishimoto, Koji Tomitsuka, Hiroyasu Sano, and Atsushi Okamura, "Approximate LLR Calculation for Spectrally-precoded Diversity Transmission," Proceedings of the 2018 IEICE General Conference, B-5-32, p.323, Tokyo, Japan, March 2018 (in Japanese).

[11] Kanako Yamaguchi, Masatsugu Higashinaka, Hiroyasu Sano, and Atsushi Okamura, "A Phase Rotated Transmit Diversity Technique with Envelope Variation Suppression for FSK," Proceedings of the 2019 IEICE General Conference, B-5-54, p.320, Tokyo, Japan, March 2019 (in Japanese).

[12] Kanako Yamaguchi, Masatsugu Higashinaka, Hiroyasu Sano, Atsushi Okamura, Takeo Ohgane, and Toshihiko Nishimura, "A Narrowband Pilot-less Coherent Detection for FSK with Transmit Diversity," Technical Report of IEICE Radio Communication Systems, RCS2019-144, pp.211–216, Osaka, Japan, July 2019.

[13] Kanako Yamaguchi, Akinori Nakajima, and Masatsugu Higashinaka, "An Envelope Variation Reduction by Applying Phase Rotated Transmit Diversity with Multiple

Antennas," Proceedings of the 2019 IEICE Society Conference, B-5-19, p.273, Toyonaka, Japan, Sept. 2019 (in Japanese).

## Awards

[1] 2017 Young Researchers' Award, IEICE, 2018.